

Review Article  
**INTERACTION OF BUBBLES WITH SOLID SURFACES**

Anh Nguyen, Jaroslaw Drelich, Miroslav Colic,  
Jakub Nalaskowski, and Jan D. Miller

**Abstract**

Interaction of bubbles with solid surfaces is considered with respect to approach/contact, film rupture, and bubble attachment, with particle separation by flotation the classic example. During approach/contact bubble deformation may occur and the interaction involves momentum transfer as described by hydrodynamic forces. Subsequent interaction involving film rupture is governed by interfacial forces including van der Waals forces, electrostatic forces, hydration forces, and hydrophobic forces. The structure and stability of the film is considered with respect to interfacial water structure and the presence of surface stabilized, nanosized gas bubbles. Featured properties of the solid surface (roughness, heterogeneity) have a significant influence on water film stability and rupture. Finally the bubble attachment is examined in terms of the three-phase line of contact, its formation and relaxation.

**1. Introduction**

Interaction of gas bubbles with solid surfaces plays an important role in many areas of technology. Most significant is the role in particle separation by the flotation process. The essence of the separation is bubble attachment to the surface of hydrophobic particles, which leads to flotation due to the buoyancy of the particle/bubble aggregate. In this way separation is achieved from other particle types which are maintained in a hydrophilic state.

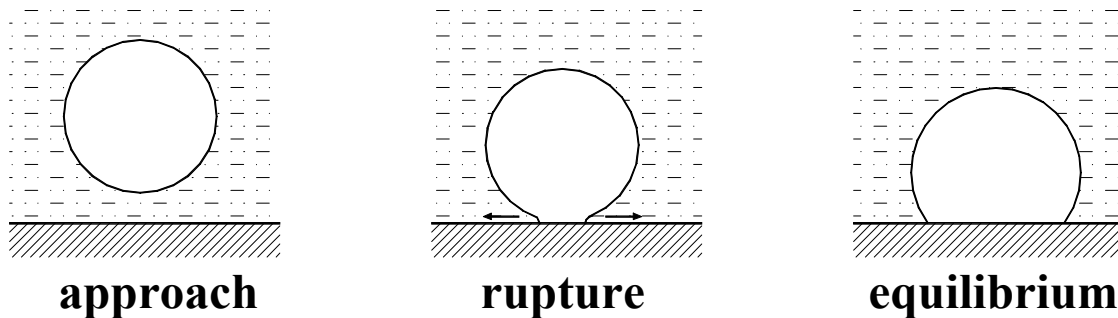


Figure 1. Sequence of events for bubble attachment at a hydrophobic surface

By no means is interaction of bubbles with solid surfaces or particles a simple process. On the contrary, it is a complicated process, which can be divided into several steps governed by different forces. See Figure 1. These steps will describe the behavior of the bubble at various distances from the solid surface during the approach and ultimate displacement of the liquid phase. The bubble-solid interaction starts at a certain distance where bubble and particle approach each other in a gravitational field or another applied force field. During this approach hydrodynamic forces between the bubble and solid surface are of great importance. On closer approach, interfacial forces become most important, governing further stability of the liquid film between the gas-liquid and solid-

liquid interfaces. Depending on the type of solid surface and the solution chemistry of the liquid phase, these forces can be repulsive, thus stabilizing the liquid film between interfaces, or they can be attractive, resulting in destabilization of the liquid film. In the latter case, the liquid film becomes unstable and ruptures, leading to the formation of a three-phase contact (TPC) line and attachment of the bubble. After rupture, the three-phase-contact line moves across the solid surface at a certain rate. This relaxation process initiated during rupture of the film leads to a stable or meta-stable state, governed by the thermodynamic properties of the gas-solid, liquid-solid, and gas-liquid interfaces as well as quality of the solid surface.

## 2. Capillary and Hydrodynamic Interactions during Approach

There is a number of reviews published on the hydrodynamic interaction during bubble-particle encounter [1-5]. The emphasis of this section is on the capillary and hydrodynamic interactions during bubble-particle contact.

The bubble-solid approach can take place with different trajectories due to their respective directions of motion. If a particle approaches a bubble in a direction normal to the bubble surface, the momentum of the approach is high, causing strong deformation of the local gas-liquid interface (Figure 2). This bubble-particle interaction is called the collision contact. Another extreme case is the sliding contact when a bubble and a particle meet each other without any significant deformation of the local bubble surface. In this case the particle usually slides on the bubble surface after initial encounter. The hydrodynamic interactions during bubble-particle approach have been modeled based on these extreme cases [6-11].

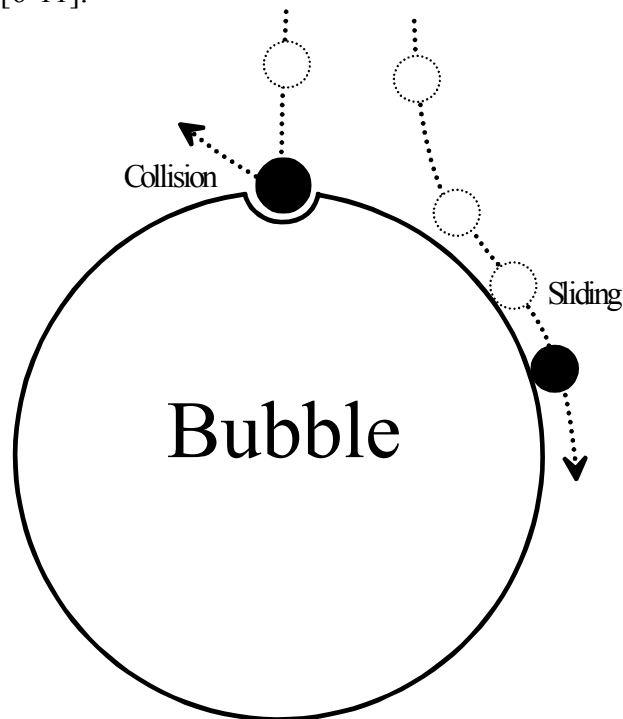


Figure 2. Illustration of the collision and sliding interactions

### Bubble deformation

Since particles are usually much smaller than bubbles in flotation, the physical picture of bubble deformation has commonly been approximated to be the deformation of a planar interface by the approach of a solid sphere (Figure 3). As shown in this figure, the deformed interface is divided into two parts, namely, the inner and outer menisci ([6, 8, 11]). The inner meniscus, where the intervening liquid film is formed, is spherical. The outer meniscus is non-spherical. These two parts of the meniscus profile are separated by the transition angle  $\alpha$  as shown by point T in Figure 3.

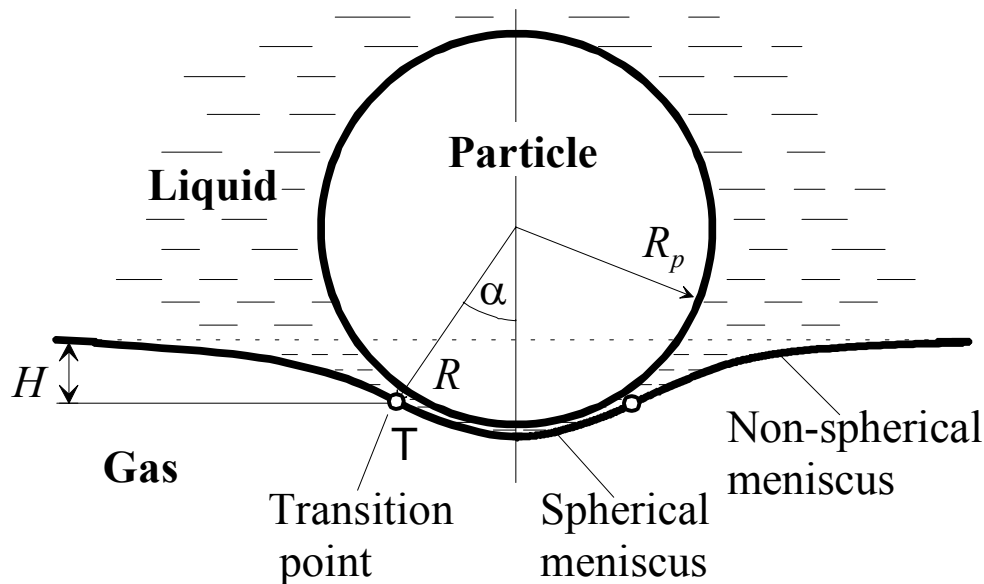


Figure 3. Deformation of a gas-liquid interface by the particle approach

The non-spherical meniscus is governed by the Young-Laplace equation, which is a second order partial differential equation and cannot be integrated in closed form for the general case of the bubble-particle interaction. It must usually be solved numerically. This is a relatively easy task for modern computers and replaces extensive tables of solutions available in the literature [12, 13], which are not convenient to use in the force analysis since an interpolation scheme is required. However, the numerical computation is still difficult to apply in the modeling exercises and a number of approximate solutions have been used to describe the shape of the non-spherical meniscus. These approximate solutions include Poisson equation for meniscus with small angular inclinations, Derjaguin equation for meniscus wrapping small particles, and empirical solutions.

The Poisson [14] equation for the meniscus depression was used to describe the meniscus of the deformed bubble surface due to particle approach by Philippoff [15]. The Poisson solution to the Young-Laplace equation was derived based on the assumption of small angular inclinations of the deformed interface so that the non-linear Young-Laplace equation can be replaced by a linear differential equation. For the depression,  $h$ , of the non-spherical meniscus the Poisson solution as a function of the radial distance,  $r$ ,

measured from the axis of symmetry gives [12]

$$\frac{h(r)}{L} = \frac{K_0(r/L)}{K_1(R \sin \alpha / L)} \tan \alpha \quad \text{Eq. 1}$$

where  $K_0$  and  $K_1$  are the modified Bessel functions of the second kind, and of zero and first order, respectively.  $R$  is the radius of the spherical meniscus, which is equal to the particle radius plus the liquid film thickness (Figure 3).  $L$  is the capillary length defined by

$$L = \sqrt{\frac{\sigma}{g\delta}} \quad \text{Eq. 2}$$

where  $\sigma$  is the surface tension,  $\delta$  is the liquid density and  $g$  is the acceleration due to gravity. For an air-water interface at 20°C ( $\delta = 1000 \text{ kg/m}^3$ ;  $\sigma = 72.8 \text{ mN/m}$ ),  $L = 2.72 \text{ mm}$ .

For the maximum depression,  $H$ , of the non-spherical meniscus substituting  $r = R \sin \alpha$  into Eq. 1 and expanding the Bessel functions into a Maclaurin series gives

$$H = R \sin^2 \alpha \left( \ln \frac{2L}{R \sin \alpha} - \gamma \right) \quad \text{Eq. 3}$$

where  $\gamma = 0.5772$  and is the Euler constant. Eq.3 was first derived by Poisson [14]. Comparison to the exact numerical results shows that both Eq. 1 and Eq. 3 are accurate up to the maximum angle of meniscus inclination at about 60°.

The Poisson equation was derived based on the assumption of the small radius  $R \sin \alpha$  at contact, but it is additionally subjected to the limit of the small angular inclination of the meniscus. Better approximations can be obtained based on the method of matched asymptotic perturbation. In this perturbation, the meniscus is mathematically separated into two characteristic regions. The region far from the contact is characterized by the small angular inclination of the deformed interface, for which the Poisson solution can be applied. The second region is close to the contact with the wrapped particle having a small radius. This close region is characterized by the short radial coordinate, for which the Young-Laplace equation can be simplified to the differential equation of the catenary and can be solved. The solutions for these two regions can be linked by matching the profiles of the menisci, leading to the following expression for the maximum depression,  $H$ , of the non-spherical meniscus:

$$H = R \sin^2 \alpha \left( \ln \frac{4L/R/\sin \alpha}{1 + \cos \alpha} - \gamma \right) \quad \text{Eq. 4}$$

This equation was first derived by Derjaguin [16]. It can be observed that the Derjaguin equation reduces to the Poisson equation in the limit of small  $\alpha$ . These

approximations are significantly different if the wrapping meniscus has a neck. Comparison to the exact numerical results shows that the relative error of the Derjaguin equation is smaller than 5% over the whole range of  $\alpha$  if  $R \sin \alpha / L \leq 0.2$ . Eq. 4 was used to describe the meniscus of the deformed bubble surface due to the particle approach by Scheludko and Schulze et al. [6, 8].

The approximate analytical solution to the Young-Laplace equation for the meniscus wrapping large contact radius “ $R \sin \alpha / L$ ” can also be developed by successive approximation schemes, starting from the solution for the meniscus around a plate [17], resulting in the following prediction for the maximum meniscus depression:

$$\frac{H}{L} = \sin(\alpha / 2) \frac{2}{\sqrt{1 + L / (R \sin \alpha)}} \quad \text{Eq. 5}$$

This equation is accurate for all  $\alpha$ , when compared with the exact numerical data, if  $R \sin \alpha / L \geq 2$ . For the intermediate range of the contact radius  $R \sin \alpha / L$  between 0.2 and 2, the solution to the Young-Laplace equation for the maximum depression of the non-spherical meniscus can be obtained by the rational empirical approximation [18], leading to

$$\frac{H}{L} = a \sin(b\alpha) \quad \text{for } 2 \geq R \sin \alpha \geq 0.2 \quad \text{Eq. 6}$$

where  $a$  and  $b$  are the empirical parameters obtained by fitting the exact numerical data to the Young-Laplace equation. The following equations were obtained:

$$a = \frac{2.186}{1 + 0.649 \left( \frac{L}{R \sin \alpha} \right)} \quad \text{Eq. 7}$$

$$b = 0.332 \exp \left( -2.122 \frac{R \sin \alpha}{L} \right) + \frac{1}{2} \quad \text{Eq. 8}$$

Comparison between the numerical results and Eq. 6 is shown in Figure 4. As seen in this figure, these equations are accurate for  $\alpha \leq 140^\circ$ . This range is useful for modeling of bubble deformation due to particle approach, attachment and detachment during flotation.

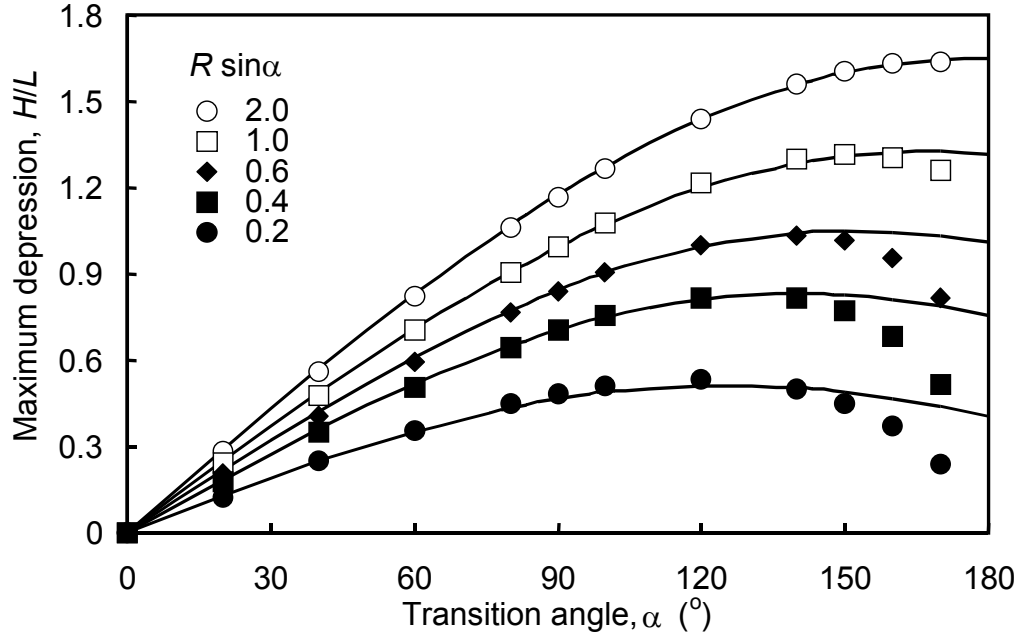


Figure 4. Comparison of Eq. 6 (solid curves) to the exact numerical results (points) for the meniscus depression for  $2.0 \geq R \sin \alpha / L \geq 0.2$  [19].

#### Film thinning and hydrodynamic forces during collision

The film thinning between a particle and a bubble is controlled by both equilibrium (intermolecular and surface) and dynamic forces. The dynamic aspects of film thinning can be examined using the continuum hydrodynamics, as commenced by Stefan and Reynolds [20], leading to the celebrated Stefan-Reynolds equation, Eq. 9, which links the hydrodynamic (resistance) force,  $F$ , and the rate,  $V$ , of film thinning by

$$F = -\frac{3\pi\mu VR^4}{2h^3} \quad \text{Eq. 9}$$

where  $R$  and  $h$  are the film radius and thickness, and  $\mu$  is the liquid viscosity. The Stefan-Reynolds equation was derived for liquid films at parallel plane surfaces, for which both  $V$  and  $h$  do not vary along the film. The Stefan-Reynolds equation was validated for free (foam) films between two bubbles, as well as wetting films between a flat solid substrate and a gas bubble by Scheludko and others [21-23]. This equation can be used, as a first approximation, to calculate the time of thinning of the local intervening water film during the bubble-particle collision interaction [24]. During interaction the hydrodynamic resistance is counterbalanced by the disjoining pressure,  $\Pi$ , of intermolecular and surface forces, the Laplace (capillary) pressure,  $P_\sigma$ , and other external (gravitational and applied) forces. Neglecting the external forces, Eq. 9 gives

$$\frac{dh}{dt} = -\frac{2h^3}{3\mu R^2} (P_\sigma - \Pi) \quad \text{Eq. 10}$$

This equation can be numerically integrated for the dependence of film thickness on time, given that the disjoining pressure as a function of film thickness is known. An example is shown in Figure 5.

Both Eq. 9 and Eq. 10 are applied to no-slip bubble surfaces. If the slip bubble surface is considered, the boundary conditions for the zero liquid velocities at the interface are replaced by zero interfacial stresses. In this case, the numerical constant  $2/3$  on the right hand side of Eq. 10 is replaced by  $8/3$ .

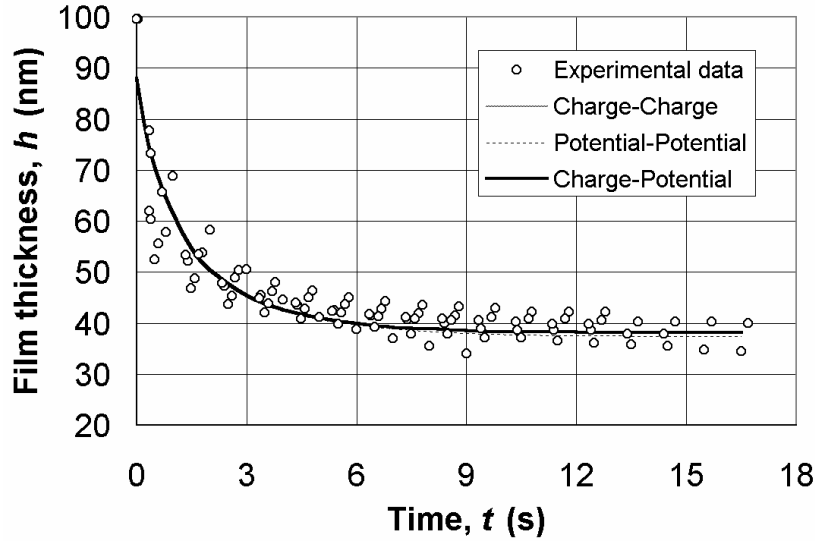


Figure 5. The Stefan-Reynolds equation (lines) and experimental (points) [25] thickness of stable planar 0.001 M KCl films between an air bubble and a hydrophilic glass surfaces versus time. The double-layer interaction are predicted using the Hogg-Healy-Fuerstenau equation [26] for the constant surface potential (potential-potential) conditions. The double-layer interactions under the other two conditions are described in the literature [27]

The effect of the curvature of the deformed (“spherical”) meniscus on the film thinning and the hydrodynamic force can also be studied using the lubrication approximation of the Navier-Stokes equations in conjunction with the continuity equation [28]. The final result for the hydrodynamic resistance as a function of the thinning rate,  $V$ , the particle radius,  $R_p$ , and the radius,  $R$ , of the deformed spherical meniscus at the apex (Figure 3) can be described by the following Taylor-like equation:

$$F = -\frac{6\pi\mu V (R_{eff})^2}{h} \quad \text{Eq. 11}$$

where the effective radius,  $R_{eff}$ , of interaction is described by the following equation:

$$R_{eff} = \frac{R_p R}{R - R_p} \quad \text{Eq. 12}$$

This equation shows that the effective radius and the hydrodynamic resistance approach infinity if the radius of curvature of the deformed spherical meniscus at the apex approaches the particle radius. An extremely strong repulsive surface force (due to hydration, double-layer or steric interactions) is required to counterbalance the hydrodynamic resistance and capillary forces. Otherwise, the deformed spherical meniscus will be ruptured if the maximum of the positive disjoining pressure is attained.

### Film thinning and hydrodynamic forces during sliding

The liquid films described in the previous sections are rotationally symmetric. During particle sliding, the liquid flow streamlines in the intervening films are no longer symmetric about the bubble-particle centerline. Modeling of the thinning of the asymmetric films during the sliding interaction usually requires a two-dimensional solution of the (Navier-) Stokes equation or its simplified lubrication approximation [29]. The lubrication approximation is usually poor and either high-order approximations or matching with the numerical results are often required for obtaining the correction terms. The numerical results for the corrected drag forces for sliding interaction are shown below.

The drag force on a small particle far from the bubble surface is well described by the Stokes law:  $\mathbf{F} = -6\pi\mu a(\mathbf{V} - \mathbf{W})$  where  $\mathbf{V}$  and  $\mathbf{W}$  are the vectors of the particle and fluid velocities, respectively. When the particle approaches a surface with an intervening liquid film, the results obtained, are described by the Stefan-Reynolds Eq. 9 and the Taylor-like Eq. 11 show that hydrodynamic resistance increases rapidly. This deviation of the hydrodynamic resistance is due to short-range hydrodynamic interactions and can be accounted for using the hydrodynamic resistance functions. The Stokes drag force is modified to give:

In the (radial) direction of the bubble-particle centerline

$$F_r = -6\pi\mu aV_r f_1 + 6\pi\mu aW_r f_2 \quad \text{Eq. 13}$$

In the (tangential) direction perpendicular to the centerline

$$F_\varphi = -6\pi\mu aV_\varphi f_3 + 6\pi\mu aW_\varphi f_4 \quad \text{Eq. 14}$$

where the subscript 'r' and 'φ' describe the radial and tangential components of the drag force and the particle and fluid velocities, and functions  $f_i$  ( $i = 1$  to 4) describe the hydrodynamic resistance functions.

When the surfaces are far apart ( $h \rightarrow \infty$ ), Eq. 13 and Eq. 14 reduce to the standard Stokes drag force equations, giving

$$f_i(h \rightarrow \infty) = 1 \quad \text{for } i = 1, 2, 3 \text{ and } 4 \quad \text{Eq. 15}$$

When  $h \rightarrow 0$ , the lubrication theory described by the Taylor-like Eq. 11 applied to sliding interaction with  $-R = R_b \square R_p$  gives

$$f_1(h \rightarrow 0) = \frac{R_p/h}{m} \quad \text{Eq. 16}$$

where  $m = 1$  and  $4$  for immobile (rigid) and mobile bubbles, respectively.

The resistance functions between the two limits can be derived from the Stokes equations. The exact equations include:

For immobile bubbles with  $R_b \ll R_p$

$$f_1 = \frac{4}{3} \sinh \alpha \sum_{n=1}^{\infty} \frac{n(n+1)}{(2n-1)(2n+3)} \times \left[ \frac{2 \sinh(2n\alpha + \alpha) + (2n+1) \sinh(2\alpha)}{4 \sinh^2(n\alpha + \alpha/2) - (2n+1)^2 \sinh^2(\alpha)} - 1 \right] \quad \text{Eq. 17}$$

$$f_2 = \frac{4 \sinh^5 \alpha}{9 \cosh^2 \alpha} \sum_{n=1}^{\infty} \frac{n(n+1)(n+1/2)^2}{\sinh^2(n\alpha + \alpha/2) - (n+1/2)^2 \sinh^2 \alpha} \quad \text{Eq. 18}$$

For mobile gas-liquid interfaces

$$f_1 = \frac{4}{3} \sinh \alpha \sum_{n=1}^{\infty} \frac{n(n+1)}{(2n-1)(2n+3)} \times \left[ \frac{4 \cosh^2(n\alpha + \alpha/2) + (2n+1)^2 \sinh^2 \alpha}{2 \sinh(2n\alpha + \alpha) - (2n+1) \sinh 2\alpha} - 1 \right] \quad \text{Eq. 19}$$

$$f_2 = \frac{f_{21} - hf_{22}}{1-h} \quad \text{Eq. 20}$$

where

$$f_{21} = \frac{4 \sinh^3 \alpha}{3 \cosh \alpha} \sum_{n=1}^{\infty} \frac{n(n+1/2)(n+1)}{\sinh(2n\alpha + \alpha) - (n+1/2) \sinh(2\alpha)} \quad \text{Eq. 21}$$

$$f_{22} = \frac{4 \sinh^5 \alpha}{9 \cosh^2 \alpha} \sum_{n=1}^{\infty} \frac{n(n+1/2)^2 (n+1)}{\sinh(2n\alpha + \alpha) - (n+1/2) \sinh(2\alpha)} \quad \text{Eq. 22}$$

In these equations,  $\alpha$  is a function of the shortest separation distance,  $h$ , between the surfaces, and is described by

$$\alpha = \text{acosh} \left\{ \frac{h}{R_p} + 1 \right\} \quad \text{Eq. 23}$$

Eq. 17 and Eq. 19 can be found in [30] while Eqs. 18 and 20-22 are recently developed in [18].

For the bubble-particle interaction modeling exercises, the resistance functions described by Eq. 17 and Eq. 22 can be replaced by simple approximate equations [27] described in Table 1. The approximate equations are weighted so that they asymptotically

reduce to the correct limits at  $h \rightarrow \infty$  and at  $h \rightarrow 0$ .

Table 1. Approximate equations for hydrodynamic resistance functions in the radial direction

No-slip gas-liquid interface	Slip gas-liquid interface
$f_1 = \left\{ 1 + (R_p/h)^{0.89} \right\}^{1.124}$	$f_1 = \left\{ 1 + (R_p/4/h)^{0.719} \right\}^{1.394}$
$f_2 = \frac{2.022 + R_p/h}{0.626 + R_p/h}$	$f_{21} = \frac{1.707 + R_p/h}{0.836 + R_p/h}$
	$f_{22} = \frac{2.656 + R_p/h}{1.440 + R_p/h}$

The hydrodynamic resistance functions in the tangential direction parallel to the bubble surface cannot be described by closed-form expressions like Eqs. 17-22 and are determined numerically [29, 31]. The calculation is also complicated by the fact that a particle in shear flow in the tangential direction is subjected to both the translational and rotational motions. The translation also generates a torque about the particle center and the rotation creates an additional drag force. For sliding particles the combined torque must be balanced by the particle internal reaction and the angular velocity can be determined. The numerical results for the resistance function for  $f_3$  are shown in Figure 6.

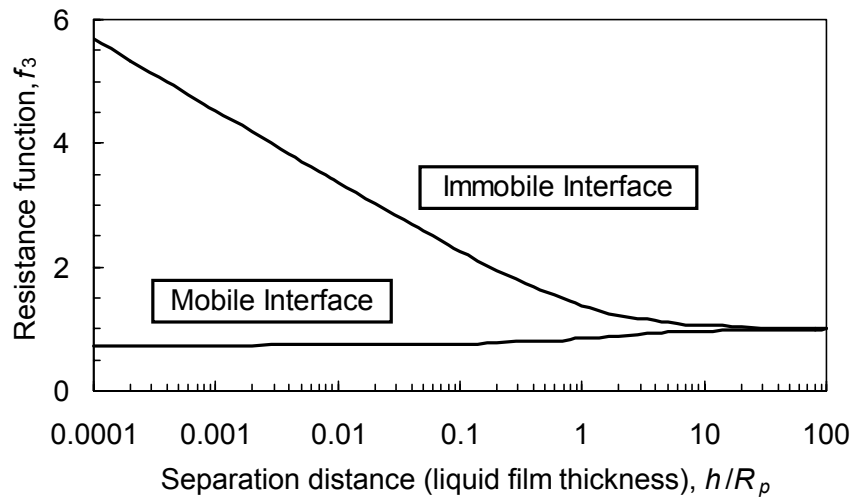


Figure 6. Hydrodynamic resistance function for immobile [29] and mobile gas-liquid interfaces

The prediction for  $f_4$  depends on the liquid shear flow in the direction tangential to the bubble surface, which may have a number of terms representing the uniform, linear or parabolic shear flows [32]. The uniform shear flow only exists at the mobile bubble

surface, where the tangential liquid velocity is non-zero. The final results for  $f_4$  can be described by

$$f_4 = \frac{W_0 f_{40} + W_1 f_{41} + W_2 f_{42}}{W_0 + W_1 + W_2} \quad \text{Eq. 24}$$

where  $W_0$ ,  $W_1$  and  $W_2$  are the uniform, linear and parabolic terms of the shear flow velocity, i.e.,  $W_\phi = W_0 + W_1 + W_2$ . The numerical results for the resistance functions  $f_{40}$  (for mobile bubbles only),  $f_{41}$  and  $f_{42}$  are shown in Figure 7.

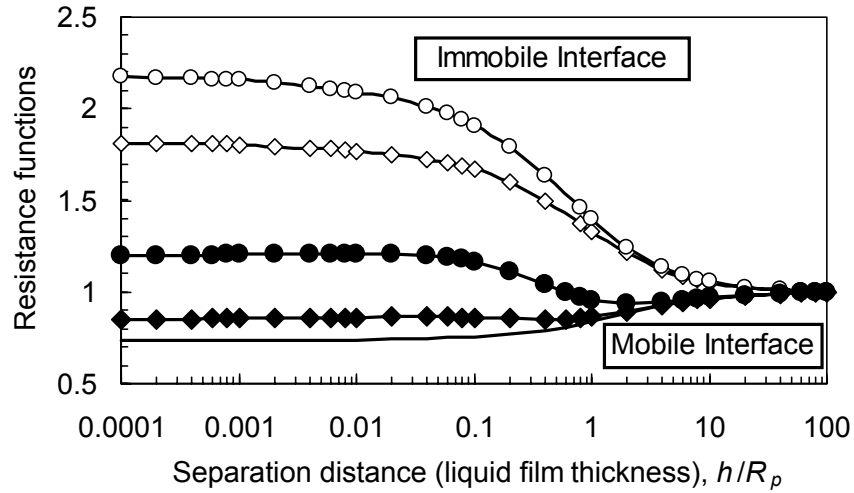


Figure 7. Hydrodynamic resistance functions  $f_{40}$  (line without symbols),  $f_{41}$  ( $\circ$  and  $\bullet$ ) and  $f_{42}$  ( $\diamond$  and  $\blacklozenge$ ) for immobile [32] and mobile interfaces

Table 2. Approximate equations for hydrodynamic resistance functions in the tangential direction

No-slip gas-liquid interface	Slip gas-liquid interface
$f_3 = \left\{ 1 + A \left\{ \ln \left[ B \left( R_p / h \right)^n + 1 \right] \right\}^p \right\}^q$	$f_3 = \frac{1.106 + h / R_p}{1.501 + h / R_p}$
$A = 0.498, B = 1.207, n = 0.986$	$f_{40} = \frac{1.107 + h / R_p}{1.502 + h / R_p}$
$p = 1.027$ and $q = 0.979$	$f_{41} = \frac{3.676 + h / R_p}{4.304 + h / R_p}$
$f_{41} = \frac{1.288 + h / R_p}{0.724 + h / R_p}$	$f_{42} = \frac{0.166 + h / R_p}{0.136 + h / R_p}$
$f_{42} = \frac{1.142 + h / R_p}{0.541 + h / R_p}$	

For the modeling of the bubble-particle interaction the numerical results shown in

Figure 6 and Figure 7 can be conveniently described by the rational approximate equations, which are given in Table 2. These approximate equations are weighted so that they asymptotically reduce to unity in the limit of  $h \rightarrow \infty$  and  $h \rightarrow 0$ .

### 3. Interfacial Forces

When a bubble approaches a solid surface, interfacial forces become significant at separation distances of about one micrometer. These forces arise from molecular interactions between charged and uncharged atoms or molecules of the interacting bodies and the surrounding medium. The forces between bodies can then be derived from the interactions between atoms or molecules and described by the force of interaction or by the energy of interaction. The energy of interaction has been used more frequently in earlier studies due to the scalar character and the possibility of comparison with the kinetic energy of molecules. However, now using direct measurement techniques, the force of interaction is determined, so in more recent works the force of interaction has mainly been used to describe the interactions for a particular system. One can transform forces values to energy, and vice versa using the Derjaguin approximation [33]. The net force between interfaces can be treated as a sum of several components acting together. The most successful approach to the problem of net interactions between two interfaces was proposed by Derjaguin, Landau, Verwey and Overbeek and is known as the DLVO theory [34, 35]. This theory treats the total interaction force between two surfaces in a liquid medium as an arithmetic sum of two components; van der Waals and electrostatic (electrical double layer) forces.

The DLVO theory has been experimentally proven by many researchers and has been found useful for explaining colloidal stability and particle behavior in aqueous solutions [36, 37]. Of course, for asymmetric systems, like the bubble and solid surface in flotation the situation is more complicated. In a great number of systems which involve a hydrophilic surface, the most important forces acting between the bubble and solid surfaces are van der Waals, and electrostatic (or electrical double layer) forces. In other cases, especially in the case of hydrophobic surfaces additional forces have to be considered, which are related to the perturbation of the water layer adjacent to the surfaces. Overlapping of the perturbed water molecules requires work to be done by or on the system, which leads to additional contributions to the DLVO forces. These solvent-structure mediated non-DLVO forces can be (repulsive) hydration forces for hydrophilic surfaces or (attractive) hydrophobic forces for hydrophobic surfaces. These forces are usually called structural forces by Derjaguin and his Russian school of surface forces [38, 39]. At short separation distances these structural forces can become oscillatory due to the entropic effects of the configurational rearrangement of solvent molecules between hydrophilic surfaces under an applied force.

#### Van der Waals Forces

Two uncharged surfaces always interact at small separation distances due to the van der Waals force. This interaction is due to the result of dipole-dipole interaction (Keesom), dipole-induced dipole interaction (Debye) or instantaneous dipole-dipole correlation (London). The forces of all three interactions between molecules decay with the seventh power of the intermolecular distance. At larger distances ( $h > 10$  nm), the

universal dispersion force decays ten times faster, due to an effect referred to as (electromagnetic) retardation. The last force (dispersive force) is always present, regardless of the interacting materials and for non-polar substances it is the most important part of the van der Waals interactions [40].

The van der Waals interaction energy can be calculated using the Hamaker approach and/or the Lifshitz approach. In the first, also referred to as the microscopic approach, the interaction force between two macroscopic bodies is calculated by a pairwise summation of all the relevant microscopic interactions, which are assumed to be non-retarded and additive. The Lifshitz approach treats each interacting material as a continuum with certain macroscopic electrodynamic properties of the interacting materials such as dielectric constants and refractive index. It is therefore often referred to as the continuum or macroscopic approach.

In the Hamaker approach energies for the interactions of all the atoms in one body with all the atoms in the other body is summed (integrated), leading to an integral expression for the interaction energy between the two macroscopic bodies,  $E$ , by

$$E = -\iiint_{V_2} \iiint_{V_1} (C \rho_1 \rho_2 / r^6) dv_1 dv_2 \quad \text{Eq. 25}$$

In Eq. 25,  $C$  is the coefficient of the appropriate interaction between elementary particles separated by distance  $r$  and  $dv_i$  ( $i = 1, 2$ ) the volume elements of bodies 1 and 2 at distance  $r$  with volumes  $V_i$ , and with densities of atoms or molecules of  $\rho_i$ . The problem appears simple since it only requires the calculation of a closed integral. However, the results in closed analytical forms are available only for some simple systems.

For bubble-particle and particle-particle interaction, the sphere-sphere interaction is of particular importance and can be expressed as follows:

$$E = -\frac{A}{6} \left\{ \frac{2R_1 R_2}{r^2 - (R_1 + R_2)^2} + \frac{2R_1 R_2}{r^2 - (R_1 - R_2)^2} + \ln \frac{r^2 - (R_1 + R_2)^2}{r^2 - (R_1 - R_2)^2} \right\} \quad \text{Eq. 26}$$

where  $R_1$  and  $R_2$  are the radii of two spheres and  $r$  the inter-center separation. The term  $A$  is termed the Hamaker constant. This formula for interaction energy is also particularly useful since, when used with the effective Hamaker constant calculated by the continuum theory, it predicts approximately the same energy versus separation distance between two spheres as the continuum theory does [41].

The Hamaker constant,  $A$ , accepts values in the range of  $10^{-21}$ - $10^{-18}$  J and is specific for a given system, although it may also be calculated from the Hamaker constants for each component, based on combining relations. For a symmetric system, the Hamaker constant  $A_{131}$  (two materials 1 interacting across a medium 3) is always positive and the van der Waals force is attractive. For an asymmetric system, it may happen that  $A_{132}$  (material 1 and material 2 interacting across a medium 3) is negative under which condition the van der Waals force is repulsive. This is the case for bubble-particle interactions during flotation. The medium effect on the van der Waals force is analogous

to the buoyancy of a body in a gravitational field [40].

The assumption of simple pairwise additivity during calculation of the Hamaker constant ignores the influence of neighbouring atoms on the interactions between pairs of interacting atoms. Also, the effect of the medium is not taken into account. Atoms at one surface also polarize atoms of the medium and such instantaneous dipoles induce dipoles at another surface. These problems are avoided in the Lifshitz theory [42], where the interaction is calculated from the bulk properties of materials including dielectric constant and refractive index.

The Lifshitz theory yields the van der Waals interaction energy  $E_{132}$  (per unit area) between two half-spaces 1, 2 immersed in a medium 3 as a function of the separation  $h$  as follows: [43]

$$E_{132}(h) = \frac{k_B T}{8\pi h^2} \sum_{n=0}^{\infty} \int_{x_n}^{\infty} x \ln[(1 - y_{13} y_{23} e^{-x})(1 - z_{13} z_{23} e^{-x})] dx \quad \text{Eq. 27}$$

$$y_{a3} = \frac{x\varepsilon_a - s_a\varepsilon_3}{x\varepsilon_a + s_a\varepsilon_3} \quad z_{a3} = \frac{x - s_a}{x + s_a} \quad \xi_n = 2n\pi k_B T / \hbar \quad x_n = 2h\xi_n \sqrt{\varepsilon_3} / c$$

$$s_a^2 = x^2 + x_n^2 \{\varepsilon_a / \varepsilon_3 - 1\} \quad \varepsilon_a = \varepsilon_a(i\xi_n)$$

In these equations, the subscript  $a = 1$  to 3,  $i = \sqrt{-1}$ ,  $c$  is the speed of light,  $k_B$  is Boltzman's constant,  $T$  is the absolute temperature,  $\hbar$  is Planck's constant divided by  $2\pi$  and  $i\xi_n$  are the discrete equally spaced imaginary frequencies. The prime on the summation symbol indicates that the zero-frequency ( $n = 0$ ) term, which accounts for the contributions due to the orientation and induction interactions, is divided by 2. Eq. 27 is somewhat complicated but it shows that the interaction energy depends on electromagnetic fluctuations, via the relative permittivity,  $\varepsilon(i\xi_n)$ , of all three materials.

At short separations Eq. 27 simplifies to

$$E_{132}(h \rightarrow 0) = \frac{k_B T}{8\pi h^2} \sum_{n=0}^{\infty} \int_{x_n}^{\infty} x \ln \left\{ 1 - \frac{\varepsilon_1 - \varepsilon_3}{\varepsilon_1 + \varepsilon_3} \frac{\varepsilon_2 - \varepsilon_3}{\varepsilon_2 + \varepsilon_3} e^{-x} \right\} dx \quad \text{Eq. 28}$$

The Hamaker constants can now be determined using the static dielectric constant and refractive index, which are easily measurable and reported in the literature for most minerals [44].

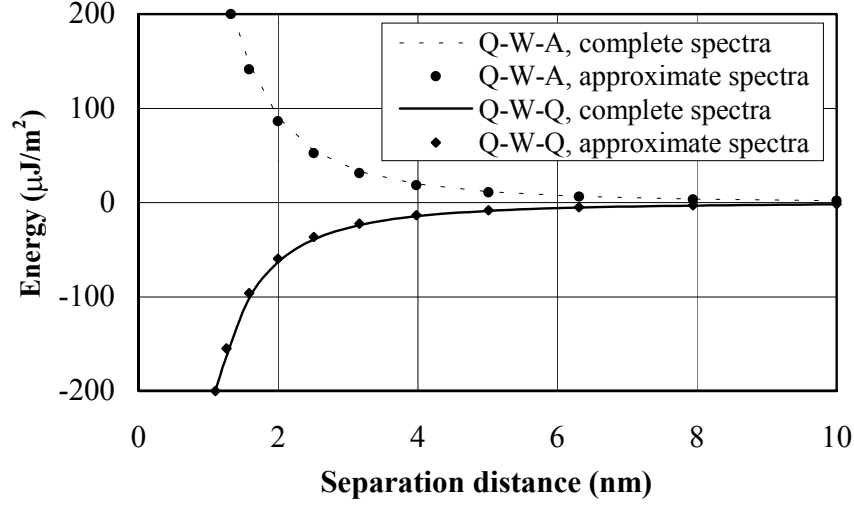


Figure 8. Van der Waals energy determined by Eq. 27 for quartz-water-air and quartz-water-quartz systems at 20°C

It has to be noted that the electromagnetic retardation manifests itself at a separation of about 3 nm. One of the best ways to involve the retardation effect is to express the Hamaker constant as function of the separation distance.

$$A_{132}(h) = -\frac{3kT}{2} \sum_{n=0}^{\infty} \int_{x_n}^{\infty} x \ln[(1 - y_{13}y_{23}e^{-x})(1 - z_{13}z_{23}e^{-x})] dx \quad \text{Eq. 29}$$

This equation reflects the dependence of the “Hamaker constant” on the separation  $h$ , as a result of electromagnetic retardation, and is referred to as the Hamaker function or the effective Hamaker constant,  $A_{132}(h)$ . One can split the expression for  $A_{132}(h)$  into two parts, namely, the zero-frequency part and the nonzero-frequency (dispersion) part, as follows:

$$A_{132}(h) = A_{132}^0 + A_{132}^{\xi}(h) \quad \text{Eq. 30}$$

It should be noted that the zero-frequency contribution,  $A_{132}^0$ , to the Hamaker constant and the Hamaker function is essentially an electrostatic interaction and will be screened if the interacting medium is an electrolyte. This results in a decrease of  $A_{132}^0$  by a factor of  $(1 + 2\kappa h)\exp(-2\kappa h)$  [43], where  $\kappa$  is the reciprocal Debye length. The screened, retarded Hamaker function is determined by

$$A_{132}(\kappa, h) = A_{132}^0(1 + 2\kappa h)e^{-2\kappa h} + A_{132}^{\xi}(h) \quad \text{Eq. 31}$$

For the modeling of bubble-particle interaction in flotation the static dielectric constants of minerals are not always available. Fortunately, the zero-frequency term

involving the dielectric constant is screened by electrolytes and may be ignored. The refractive index of minerals available from mineralogical studies is sufficient for the determination of the Hamaker function in the analysis of flotation systems.

### Electrostatic (Electrical Double Layer) Forces

In a polar solvent, like water, most surfaces, including air bubbles and solids, become electrically charged. The charge can arise from preferential hydration of lattice ions, dissociation of ionizable groups present such as OH groups at oxide surfaces, or by adsorption/reaction of ions at a surface. The degree of ionization depends on the chemistry of the surface and may be different for different materials and solution conditions (pH, temperature).

Ions with charge opposite to that on the surface (counterions) are attracted, while ions with the same charge (co-ions) are repelled from the surface. As a result, the concentration of ions next to the surface is different from that in the bulk. This layer of ions is referred to as the diffuse layer, which together with the layer of adsorbed ions, composes the so-called electrical double layer (EDL), see Figure 9.

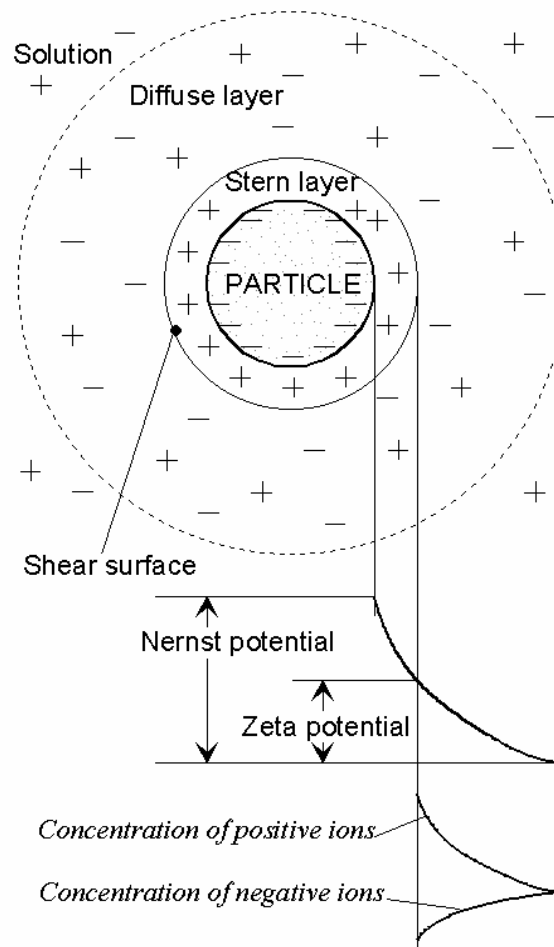


Figure 9. Electrical double-layer (EDL) around a particle

The important parameter which measures the thickness of double layer, is called the Debye constant,  $\kappa$ , and is mathematically described by

$$\kappa = \left\{ \frac{e^2 \sum n_i(\infty) z_i^2}{\epsilon \epsilon_0 k_B T} \right\}^{1/2} \quad \text{Eq. 32}$$

where  $e$  is the charge on electron,  $n_i(\infty)$  is the number per unit volume of the electrolyte ions of type  $i$  with valence  $z_i$  in the bulk solution far from the surface,  $k_B$  is Boltzmann's constant,  $T$  is the absolute temperature (in Kelvin),  $\epsilon_0$  is the permittivity of vacuum, and  $\epsilon$  is the relative permittivity (the dielectric constant) of the solution ( $\epsilon = 80$  for ordinary water). The summation is over all the electrolyte ions in solution. For water at 25°C, one has  $\kappa = 3.288\sqrt{I}$  where  $\kappa$  is measured in  $\text{nm}^{-1}$  while both the ion concentration  $c_i$  and the ionic strength  $I$  are measured in mol/L. Typical values of  $1/\kappa$  range from a fraction of a nanometer to about 200 nm.

When two similarly charged surfaces approach each other the overlap of the EDLs produces a repulsive force. When surfaces are oppositely charged, overlapping of the EDLs produces attraction. The force between two surfaces can be calculated from the non-linear Poisson-Boltzmann equation describing the electrostatic potential around a surface in an ionic solution.

$$\epsilon \epsilon_0 \nabla^2 \psi = -e \sum z_i n_i(\infty) \exp \left\{ -\frac{e z_i \psi}{k_B T} \right\} \quad \text{Eq. 33}$$

This equation (where  $\psi$  is a surface potential) is the basis of the Gouy-Chapman theory of the electrical double layer, which assumes that the solvent is a structureless continuum, the ions are point charges, and the potential of the mean force and the average electrostatic potential are the same. A substantial amount of theoretical work has been done to identify the limitations of these assumptions. However, experiments [45] have shown that the Poisson-Boltzmann equation works surprisingly well down to separations of a few nanometers.

The force of the electrical double-layer interaction also depends on the charging mechanisms occurring at the surfaces during the interaction. The following three cases are usually considered; the surface potential remains constant, the surface charge remains constant, and the surface charge and potential change by a charge regulation.

This particular aspect of charge regulation is not well established in flotation. If a particle slides over the bubble surface, the location of the particle-bubble interaction changes continuously. In this case, a perfect regulation of surface charge is difficult to establish and the interaction at constant surface charge is more appropriate than the interaction at constant surface potential. A perfect regulation of charge may take place if the location of the bubble-particle interaction does not change over the bubble surface. Thus, the constant surface potential interaction probably occurs during the bubble-particle collision interaction.

The electrical double-layer interaction between surfaces is best solved by numerical methods because of the non-linearity of the Poisson-Boltzmann equation. The linear

(Debye-Hückel) approximation is used for weakly charged surfaces, i.e. when the reduced potential is significantly small. The Derjaguin approximation is applicable for separations smaller than the radius of the spheres. The superposition approximation is used when the surfaces are far apart, i.e., when the scaled separation is significantly greater than one. These approximations are often used in a number of combinations. The linear Debye-Hückel approximation has a wide range of applicability and is convenient for modeling bubble-particle interactions.

The disjoining pressure between two flat electrical double layers at a distance  $h$  is equal to the sum of a repulsive osmotic term and an attractive electrical stress contribution. In the framework of the linearized Debye-Hückel approximation the disjoining pressure can be expressed as:

$$\Pi(h) = \frac{\varepsilon\varepsilon_0\kappa^2\psi^2}{2} - \frac{\varepsilon\varepsilon_0}{2} \left\{ \frac{d\psi}{dx} \right\}^2 = 2\varepsilon\varepsilon_0\kappa^2 c_1 c_2 \exp(-\kappa h) \quad \text{Eq. 34}$$

Integrating the disjoining pressure from  $h$  to infinity gives the interaction energy (per unit area) between the plates, which can be inserted into the Derjaguin approximation to obtain the force and energy of the double-layer interaction between a bubble and a solid particle, leading to

$$F(h) = \frac{2\pi R_b R_p}{R_b + R_p} \int_h^\infty \Pi(y) dy \quad \text{Eq. 35}$$

$$E(h) = \frac{2\pi R_b R_p}{R_b + R_p} \int_h^\infty F(y) dy \quad \text{Eq. 36}$$

In these equations,  $y$  is a new integration variable. When inserting, for instance, Eq. 34 into Eq. 35,  $h$  is replaced by  $y$ . Note that the integrals cannot be evaluated at this stage because the integration constants  $c_1$  and  $c_2$  are functions of the separation distance between the plates. This function is obtained using the surface charging mechanisms.

At constant surface potentials the equations for the integration constants, the disjoining pressure, and the force and energy between a bubble and a particle are described by

$$c_1 = \frac{\psi_1 \exp(\kappa h) - \psi_2}{2 \sinh(\kappa h)} \quad c_2 = \frac{\psi_2 \exp(\kappa h) - \psi_1}{2 \sinh(\kappa h)}$$

$$\Pi^\psi = \frac{\varepsilon\varepsilon_0\kappa^2}{2} \frac{2\psi_1\psi_2 \cosh(\kappa h) - \psi_1^2 - \psi_2^2}{\sinh^2(\kappa h)} \quad \text{Eq. 37}$$

$$F^\psi = \varepsilon\varepsilon_0\kappa \frac{2\pi R_b R_p}{R_b + R_p} \frac{2\psi_1\psi_2 \exp(\kappa h) - \psi_1^2 - \psi_2^2}{\exp(2\kappa h) - 1} \quad \text{Eq. 38}$$

$$E^\psi = \frac{\varepsilon\varepsilon_0\pi R_b R_p}{R_b + R_p} [4\psi_1\psi_2 \operatorname{atanh}(e^{-\kappa h}) + (\psi_1^2 + \psi_2^2) \ln(1 - e^{-2\kappa h})] \quad \text{Eq. 39}$$

During the interaction at constant surface potentials, two surfaces having potentials of unlike sign ( $\psi_1\psi_2 < 0$ ) are attracted to each other at all separation distances as expected. If the surfaces have potentials of like sign but of unequal magnitude, the interaction is repulsive at large separations but attractive at small separations. In the case of like sign potentials of equal magnitude, the surfaces are repelled at all separations.

The condition of the interaction may be such that, instead of potentials, charge per unit area on the surfaces (charge densities)  $\sigma_1$  and  $\sigma_2$  remains constant. The integration constants yield

$$c_1 = \frac{\sigma_1 \exp(\kappa h) + \sigma_2}{2\kappa\varepsilon\varepsilon_0 \sinh(\kappa h)} \quad c_2 = \frac{\sigma_1 + \sigma_2 \exp(\kappa h)}{2\kappa\varepsilon\varepsilon_0 \sinh(\kappa h)}$$

The charge densities for the constant charge interaction can be calculated using the potentials of the (isolated) plates before the interaction,  $\psi_{i\infty}$  ( $i = 1, 2$ ), as follows:

$$\sigma_i = \sigma_i = -\varepsilon\varepsilon_0 (d\psi_i / dx)_{x \rightarrow 0} = \varepsilon\varepsilon_0 \kappa \psi_{i\infty} \quad \text{Eq. 40}$$

Which gives:

$$\Pi^\sigma = \frac{\varepsilon\varepsilon_0 \kappa^2}{2} \frac{2\psi_{1\infty}\psi_{2\infty} \cosh(\kappa h) + \psi_{1\infty}^2 + \psi_{2\infty}^2}{\sinh^2(\kappa h)} \quad \text{Eq. 41}$$

$$F^\sigma = \varepsilon\varepsilon_0 \kappa \frac{2\pi R_b R_p}{R_b + R_p} \frac{2\psi_{1\infty}\psi_{2\infty} \exp(\kappa h) + \psi_{1\infty}^2 + \psi_{2\infty}^2}{\exp(2\kappa h) - 1} \quad \text{Eq. 42}$$

$$E^\sigma = \frac{\varepsilon\varepsilon_0\pi R_b R_p}{R_b + R_p} [4\psi_{1\infty}\psi_{2\infty} \operatorname{atanh}(e^{-\kappa h}) - (\psi_{1\infty}^2 + \psi_{2\infty}^2) \ln(1 - e^{-2\kappa h})] \quad \text{Eq. 43}$$

The surface potential versus  $h$ , yields

$$\psi_i = \psi_{i\infty} \coth(\kappa h) + \psi_{j\infty} \operatorname{cosech}(\kappa h) \quad \text{Eq. 44}$$

The double-layer interaction between surfaces at constant charges of like sign is monotonically repulsive at all separation distances. The interaction between surfaces with opposite signs of charge is attractive at large separations and turns to repulsion at small separations.

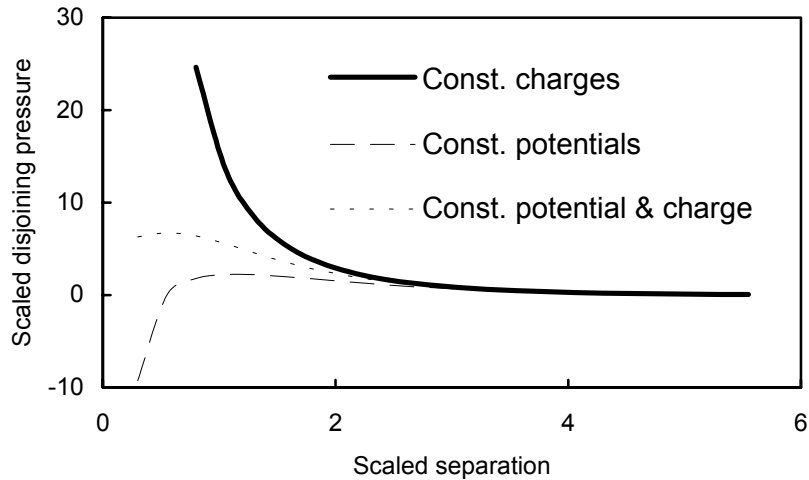


Figure 10. Isotherms of disjoining pressure (divided by  $\epsilon\epsilon_0\kappa^2$ ) between plates with different charging mechanisms

As is shown on Figure 10, the double-layer interactions are different for systems, which have the same initial potential but differ in the charging mechanism of the surfaces. In practice, neither the constant surface potential nor constant surface charge assumption is likely to be correct, mainly because of the presence of Stern layers and the uncertainty over which potential is relevant to the bubble-particle interaction. Nevertheless, the two cases of both surfaces at constant charge or constant potential may be regarded as extremes. All possible isotherms fall within a “fork” formed by the curves calculated for both surfaces at constant potential and at constant charge (Figure 10). Repulsion is minimal in the first case, and maximal in the second case.

The surface potential is required in the calculation of the double-layer interaction and is often substituted by the zeta potential,  $\zeta$ , which is the potential measured at the slipping plane by electrokinetic methods, such as electrophoresis, electroosmosis, or streaming potential. In flotation, the zeta potentials of fine minerals are mainly measured by electrophoretic methods. A comprehensive collection of the electrokinetic potential of minerals was prepared by Ney [46].

Measuring the  $\zeta$ -potentials of gas bubbles is more difficult than those of solid particles. Conventional microelectrophoretic cells have been used to measure the  $\zeta$ -potentials of microbubbles [47-51]. Taggart [52] and Saulnier et al. [53]. used a spinning horizontal cylinder to capture a bubble along the axis of its rapid rotation and measure the bubble mobility as a function of the applied voltage. The streaming current technique also has been used to determine the sign and magnitude of bubble charge relevant for flotation systems [54].

In general, gas bubbles are negatively charged in pure water and solutions of inorganic electrolytes such as NaCl and KCl (Figure 11). It can be seen that gas bubbles are negatively charged at  $\text{pH} > 2 - 3$ . The isoelectric point would be somewhere between  $\text{pH}=1.5$  and  $2.5$ . The negative  $\zeta$ -potential of bubbles at  $\text{pH} > 3$  in water indicates that  $\text{OH}^-$  ions preferentially adsorb at the clean gas-water interface.

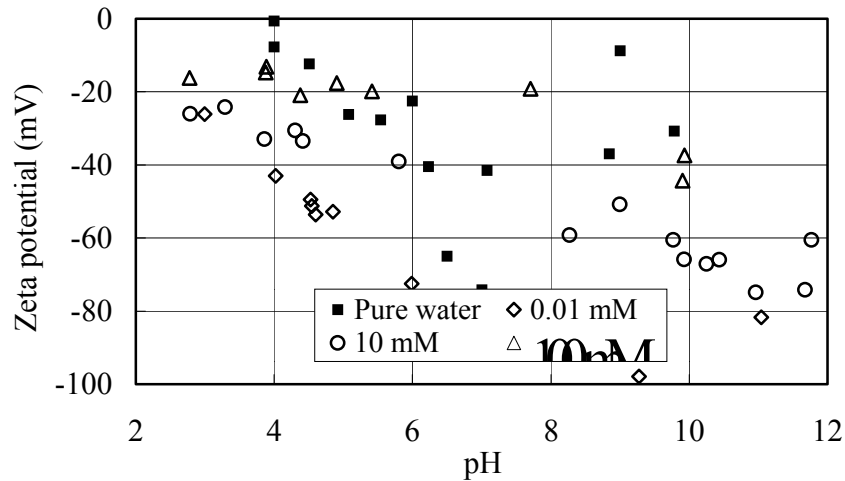


Figure 11. Zeta potential of air bubbles versus pH in water and in indifferent inorganic salt (NaCl and KCl) solutions (From [47, 55-57].)

The negative charge of gas bubbles in inorganic salt solutions can be reduced or even reversed by the addition of multivalent inorganic salts (Figure 12). This is attributed to the precipitation of hydroxides of multivalent cations at the gas-water interface in the alkaline pH region and the specific adsorption of the multivalent cations in the acidic pH range.

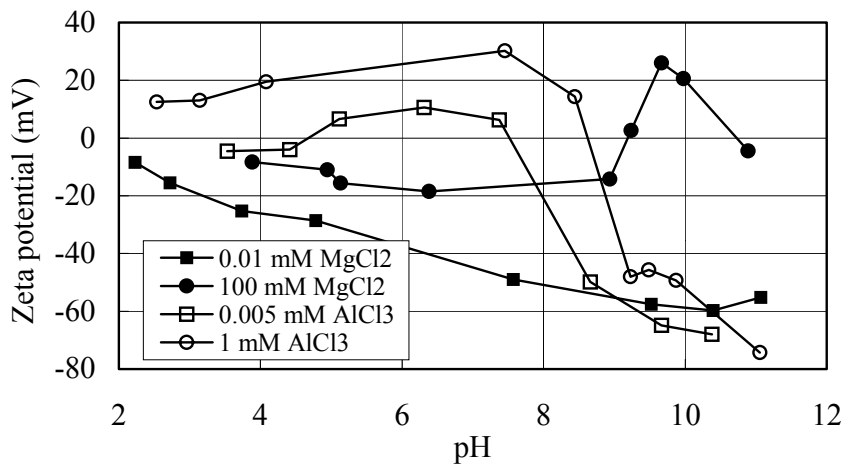


Figure 12. Effect of multivalent inorganic salts on the zeta potential of microbubbles in NaCl background solutions (From [47-49].)

In the presence of surfactants, the  $\zeta$ -potential of gas bubbles is determined by the kinetics and the adsorption/desorption/dissociation of surfactant molecules at the bubble surface. In the solution of a strongly dissociable surfactant, the  $\zeta$ -potential of gas bubbles

is determined by the type of surfactant, being negative in the presence of an anionic surfactant and positive in the presence of a cationic surfactant (Figure 13). In the presence of a weak electrolyte surfactant, the  $\zeta$ -potential may be, depending on pH, either negative or positive (Figure 14).

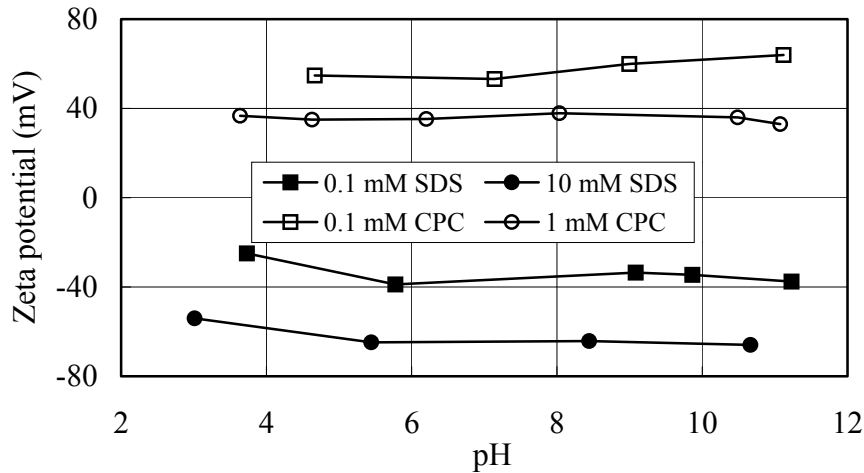


Figure 13. Zeta potential of microbubbles in solutions of strong electrolyte surfactants. SDS = sodium dodecylsulfate; CPC = cetylpyridinium chloride (From [50, 57].)

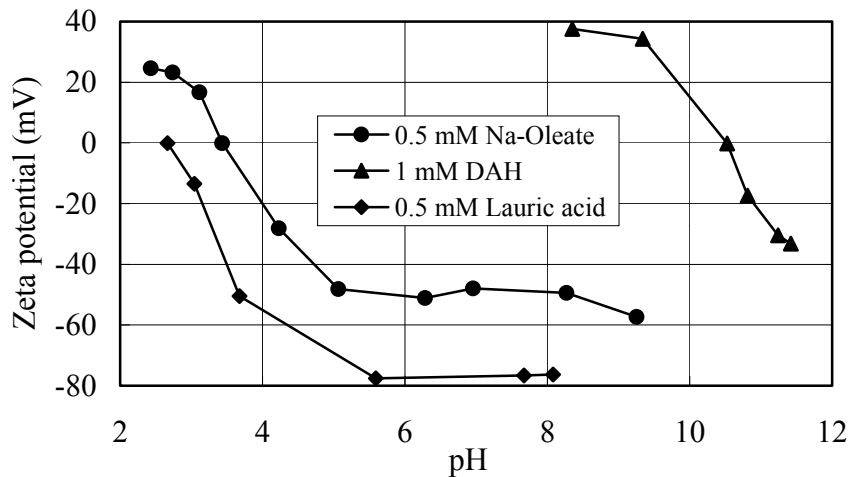


Figure 14. Zeta potential of microbubbles in solutions of weak electrolyte surfactants. DAH = dodecylamine hydrochloride (From [50, 51].)

Detailed knowledge of the effect of bubble size on the bubble  $\zeta$ -potential is not available yet, probably because of limitations of the available measuring techniques. The zeta potential of microbubbles measured with electrophoretic techniques is assumed independent of the bubble size. However, the experimental data of Usui [58] shows that

the zeta potential of bubbles measured using the Dorn effect technique increases with the bubble size, though hydrodynamic considerations complicate the interpretation of this result. Similar results were also reported by McShea and Callaghan [56] who used the spinning cylinder electrophoretic technique to measure the zeta potential. This may indicate that the  $\zeta$ -potential of air bubble depends on the physicochemical hydrodynamics of the gas-liquid interface.

### Hydration Forces

Hydration forces have been extensively studied between clay, mica and silica surfaces [36, 59, 60]. These surfaces swell spontaneously or repel each other in aqueous solutions even of very high salt concentration. In these systems, the surfaces and particles remain in strong adhesion or coagulate in a primary minimum only if the forces were the DLVO forces.

One [61] of the first attempts to predict the hydration forces is based on the expansion of the free energy density introduced by Landau in the theory of phase transitions [62]. The order parameter is defined in such a way that it is zero in a disordered (isotropic) bulk phase and nonzero (positive or negative) in the intervening liquid film. The order parameter is obtained by retaining only the first two terms in the expansion of free energy density. For the disjoining pressure, the final solution gives

$$\Pi_{hydration}(h) = (K/\lambda) \exp(-h/\lambda) \quad \text{Eq. 45}$$

where  $h$  is the separation distance,  $\lambda$  is the decay length and  $K$  is a constant. The force between two spheres is then described by

$$F_{hydration} = 2\pi \frac{R_1 R_2}{R_1 + R_2} K \exp(-h/\lambda) \quad \text{Eq. 46}$$

The order parameter is the polarization of the dielectric induced by the electric field produced by monolayers of adsorbed dipole molecules oriented perpendicular to the surface [63]. The interpretation of the order parameter as the state of polarization of water layers can be further elaborated considering the dependence of polarization in the surface layer of water molecules on film thickness [64]. The interaction force is a complicated function of  $h$  at a small thickness. At large thicknesses the hydration force can again be approximated by a single exponential function described by Eq. 46.

The phenomenological theory on structural repulsion described by Eq. 46 is confirmed by experimental data, which leads to the conclusion that the hydration force decays exponentially [36, 65]. In some situations, in place of a single exponential, a double exponential function describes the experimental data better [60]. A summary of values for the hydration force constants and decay lengths reported by various authors is given in Table 3. As can be seen from this table, for mineral systems the force constant,  $K$ , has values generally in the range  $10^{-2} - 10^{-3}$  N/m with decay lengths of the order of 1 nm when expressed in single exponential form. Hydrophilic biological systems display a higher force constant over a shorter range.

Table 3. Experimentally determined values of the hydration force constant  $K$  and decay length  $\lambda$  for symmetric systems

System	$K$ (N/m)	$\lambda$ (nm)	Reference
Mica in $10^{-4} - 10^{-2}$ M $\text{KNO}_3$	$10^{-2}$	1.0	[66]
Mica in $5 \times 10^{-4}$ M $\text{NaCl}$	$1.4 \times 10^{-2}$	0.9	[36]
Mica in $5 \times 10^{-3}$ M $\text{NaCl}$	$2.7 \times 10^{-3}$	0.9	[36]
Quartz in $10^{-3}$ M $\text{KCl}$	$8 \times 10^{-4}$	1.0	[39]
Quartz in $10^{-4}$ M $\text{KCl}$	$10^{-3}$	1.0	[39]
Glass in $10^{-4}$ M $\text{KCl}$	$1.3 \times 10^{-3}$	0.85	[39]
Montmorillonite in $10^{-4}$ M $\text{NaCl}$	$4.4 \times 10^{-3}$	2.2	[39]
Egg lecithin	$1.8 \times 10^{-1}$	0.25	[67]
Lecithin	$1.4 \times 10$	0.193	[67]

A series of experiments with molecularly smooth mica surfaces [36, 60] to identify the factors that regulate hydration forces showed that the hydrated cations bind with the negatively charged surfaces and give rise to a repulsive hydration force. This is due to the energy needed to dehydrate the bound cations, which presumably retain some of their water of hydration on binding. The strength and range of the hydration forces increase with the adsorption and degree of hydration of the adsorbing cations, following the anti-lyotropic or anti-Hofmeister series:  $\text{La}^{3+} > \text{Mg}^{2+} > \text{Ca}^{2+} > \text{Li}^+ \sim \text{Na}^+ > \text{K}^+ > \text{Cs}^+$  [60], which reflects the size and polarizability of ions as well as their mobility. Thus at saturation adsorption the weakest forces can be found with  $\text{Cs}^+$  as the adsorbing ion, the strongest with  $\text{La}^{3+}$ . Similar trends are observed with other negatively charged colloidal surfaces.

The hydration force between two mica surfaces is monotonically repulsive below about 5 nm. Below a separation distance of about 1.5 nm an oscillation with a mean periodicity of about 0.25 nm is observed, roughly equal to the diameter of the water molecule [60].

Since hydration forces can be modified and regulated by exchanging ions of different hydration states at surfaces, the influence of electrolytes on the stability of colloidal dispersions and interactions becomes complicated. In many cases, particles can be coagulated and flocculated by increasing the electrolyte concentration – an effect that was traditionally attributed to the reduced screening of the electrostatic double-layer repulsion between the particles due to the reduced Debye length. However, an increase in the electrolyte concentration may lead to the increased hydration repulsion experienced by certain surfaces when they bind highly hydrated ions at higher salt concentrations. This hydration regulation of adhesion and interparticle forces is an important practical method for controlling various processes such as clay swelling, ceramic processing and rheology, and colloidal particle and bubble adhesion and coalescence.

#### “Hydrophobic” Forces - Theory

The wetting behavior of hydrophobic solids with contact angles above zero, coagulation studies, and flotation experiments gave an early indication of the existence of a non-DLVO attractive surface force. This interaction force has been directly measured

as will be discussed later. It can be concluded from previous sections that classical theories of surface forces such as EDL or van der Waals forces cannot predict the origin of the attractive force between a solid surface and a bubble. An additional attractive surface force that can disrupt the water film and lead to the attachment of two hydrophobic particles and/or hydrophobic particle and a gas bubble has to be invoked.

Hydrophobic surfaces are inert to water in the sense that they are unable to interact or bind with water via hydrogen bonds. Hydrophobic forces between macroscopic hydrophobic surfaces have generally been found to increase with the hydrophobicity of surfaces, as conventionally defined by the contact angle of water at these surfaces. Further, the hydrophobic interaction has been found to be far stronger than the van der Waals attraction between surfaces (extending to distances of at least 10 to 100 nm), and cannot be simply a negative form of the monotonically repulsive hydration force between hydrophilic surfaces.

At present there has been no consensus on the explanation of the hydrophobic attractive forces despite a number of proposed mechanisms, which include:

- Entropic origin, arising from configurational rearrangement of the (vicinal) water molecules at the hydrophobic surfaces [68-70],
- Separation-induced phase transition (cavitation) [65, 71-73],
- Hydrodynamic fluctuating correlation [74],
- Charge-fluctuation correlation [75],
- Electrostatic origin [76, 77],
- Anomalous polarization of vicinal water molecules [78], and
- Bridging submicron bubbles [79, 80].

The prediction of hydrophobic attractive forces remains a formidable challenge to theoreticians and at present only empirical equations has been used to fit experimental data.

For many short-range hydrophobic attractive forces, data can best be fitted by a single exponential function,

$$\frac{F_{hydrophobic}}{R} = K \exp(-h/\lambda) \quad \text{Eq. 47}$$

where the decay length  $\lambda$  is about 1 nm and  $K$  is negative.

As it will be shown later, longer range hydrophobic forces have been also measured. The key feature of these measurements was that a single exponential decay law did not fit the experimental data and a double exponential function of two decay lengths

$$\frac{F_{hydrophobic}}{R} = K \exp(-h/\lambda) + K^* \exp(-h/\lambda^*) \quad \text{Eq. 48}$$

was found to give the best fit to the experimental data. The first term is called the short-range hydrophobic attraction with a decay length of 1.2 nm and the second is referred to as the long-range hydrophobic attraction

Alternatively, the measured hydrophobic force can be described by a power law

[69, 81],

$$\frac{F_{hydrophobic}}{R} = \frac{K}{h^2} \quad \text{Eq. 49}$$

which has the same form as the expression for the van der Waal forces. Experimental data shows [81] that the force constant in Eq. 49 for the hydrophobic interaction between macroscopic surfaces 1 and 2 in a medium 3 can be predicted using the geometric mean, and is a function of the contact angles,  $\theta_1$  and  $\theta_2$ , of the surfaces,

$$K_{132} = -\exp\left(a \frac{\cos\theta_1 + \cos\theta_2}{2} + b\right) \quad \text{Eq. 50}$$

where the empirical constants  $a$  and  $b$  can be obtained from a best fit of the experimental data. If the force constant is expressed in joules, the best fit gives  $a = -7.0$  and  $b = -18.0$  [81].

One of the recent approaches to further describe the hydrophobic interactions between a particle and a bubble is based on the Lifshitz-van der Waals Lewis acid-base interaction theory developed by van Oss, Good and Chaudhury [82-84]. This theory and controversy around it are reviewed and discussed by Della Volpe and Siboni [85], and will not be repeated here.

According to van Oss et al. [82-84], the total free energy of interaction between two flat and parallel surfaces or interfaces, e.g., gas-water and solid-water, can be divided into three components:

$$\Delta G_{SLG}(l) = \Delta G_{SLG}^{LW}(l) + \Delta G_{SLG}^{EL}(l) + \Delta G_{SLG}^{AB}(l) \quad \text{Eq. 51}$$

where  $\Delta G_{SLG}^{LW}$ ,  $\Delta G_{SLG}^{EL}$  and  $\Delta G_{SLG}^{AB}$  are the Lifshitz-van der Waals, electrostatic, and Lewis acid-base components, respectively, of the free energy of interaction between a solid (S) and a gas (G) through a liquid (L) expressed as a function of distance ( $l$ ) between interacting surfaces.

Lifshitz-van der Waals forces are caused by interactions between dipoles and induced dipoles. The electrostatic interaction is due to the electrical surface charge that is present on almost all interfaces surrounded by a polar liquid. Both  $\Delta G_{SLG}^{LW}$  and  $\Delta G_{SLG}^{EL}$  components come together in the classical DLVO model reviewed in previous sections. Discussion in this section is limited to the Lewis acid-base interactions that according to van Oss et al. [83, 84] are responsible for the “hydrophobic effects” observed between interacting hydrophobic surfaces; those known as being only partially wetted by water. Attraction between hydrophobic surfaces in a polar liquid arises from the fact that the liquid-liquid interactions are much more favorable than liquid-hydrophobic surface interactions.

The  $\Delta G_{SLG}^{AB}$  value of interaction between flat and parallel solid-liquid and liquid-gas interfaces as a function of distance is defined according to van Oss et al. as:

$$\Delta G_{SLG}^{AB}(l) = \Delta G_{SLG}^{AB}(l_0) \exp\left(\frac{l_0 - l}{\lambda}\right) \quad \text{Eq. 52}$$

$$\Delta G_{SLG}^{AB}(l_0) = \Delta G_{SL}^{AB} + \Delta G_{LL}^{AB} = 2(\sqrt{\gamma_S^- \gamma_L^+} + \sqrt{\gamma_S^+ \gamma_L^-}) - 4\sqrt{\gamma_L^- \gamma_L^+} \quad \text{Eq. 53}$$

where  $l_0$  is the distance between surfaces at contact,  $l_0=0.157\pm 0.009$  nm;  $\lambda$  is the correlation length for the liquid medium,  $\lambda= 0.6$  nm to 1 nm for water;  $\gamma$  is the surface/interfacial free energy component of the condensed phase; subscripts  $S$  and  $L$  refer to solid and liquid surfaces; and superscripts  $-$  and  $+$  refer to the electron donor (Lewis base) parameter and electron acceptor (Lewis acid) parameter of a surface/interface.

The  $(^+)$  and  $(^-)$  components of surface free energy, together with the Lifshitz-van der Waals component ( $^{LW}$ ), were determined for a number of liquids and solids based on contact angle measurements and several examples are shown in Tables 4 and 5.

Table 4. Surface tension (surface free energy) components for selected liquids [83]

Liquid	$\gamma_L$ [mJ/m <sup>2</sup> ]	$\gamma_L^{LW}$ [mJ/m <sup>2</sup> ]	$\gamma_L^-$ [mJ/m <sup>2</sup> ]	$\gamma_L^+$ [mJ/m <sup>2</sup> ]
Benzene	28.85	28.85	2.7	0
Diiodomethane	50.8	50.8	~0	0
Dodecane	25.35	25.35	0	0
Ethanol	22.4	18.8	~68	~0.02
Ethyl acetate	25.2	25.2	13.1	0
Ethylene glycol	48	29.0	47.0	1.9
Formamide	58	39	39.6	2.28
Glycerol	64	34	57.4	3.92
Heptane	20.14	20.14	0	0
Methanol	22.5	18.2	~77	~0.06
N-Octanol	27.5	27.5	18.0	0
Water	72.8	21.8	25.5*	25.5*

Table 5. Surface free energy components for selected solids [83, 84]

Solid	$\gamma_s$ [mJ/m <sup>2</sup> ]	$\gamma_s^{LW}$ [mJ/m <sup>2</sup> ]	$\gamma_s^-$ [mJ/m <sup>2</sup> ]	$\gamma_s^+$ [mJ/m <sup>2</sup> ]
Alumina	39.7	31.6	27.2	0.6
Apatite	35.4	35.4	20.5	0
Calcite	57	40.2	54.4	1.3
Dolomite	42.5	37.6	30.5	0.2
Hematite	53.4	45.6	50.4	0.3
Rutile	47.1	40.8	32.8	0.3
Lactose	41.1	41.1	26.8	0
Maltose	44.9	41.3	63.7	0.05
Polyethylene	33	33	0	0
Polyisobutylene	25	25	0	0
Polymethyl methacrylate	40	40	14.6	0
Polystyrene	42	42	1.1	0
Polyvinyl alcohol	42	42	17-57	0
Polyvinyl chloride	43.8	43	3.5	0.04

Combination of these parameters is frequently used for determination of the surface free energy of a solid or liquid ( $\gamma_i$ ),

$$\gamma_i = \gamma_i^{LW} + 2\sqrt{\gamma_i^+ \gamma_i^-} \quad \text{Eq. 54}$$

A negative value of  $\Delta G_{SLG}^{AB}$  calculated from Eq. 52 and Eq. 53 indicates attraction of a solid particle to a bubble surface due to acid-base type of interactions present between liquid molecules ( $\Delta G_{LL}^{AB}$ ) that are stronger than acid-base interactions between solid surface and liquid ( $\Delta G_{SL}^{AB}$ ). If also  $\Delta G_{SLG}^{AB} > \Delta G_{SLG}^{LW}$  the particle-liquid-gas system is thermodynamically unstable, at least at short separations; this instability of the system is often referred to a “hydrophobic effect”. Solid particles having hydrophobic surfaces such as most of the polymers, coal, graphite, molybdenite, sulfur, stibnite, poryphyllite, talc, and probably several other inorganic materials, all demonstrate affinity to gas bubbles in water. The “hydrophilic” solid particles (majority of the natural and synthetic inorganic solids) on the other hand, need to be modified with organic “hydrophobic” collectors to decrease the  $\gamma_s^+$  and  $\gamma_s^-$  values for solid surfaces and thus reduce or eliminate attractive Lewis acid-base interactions between solid surface and liquid. Strong solid-liquid Lewis acid-base interactions enhance stability of the liquid film separating a solid particle from a gas bubble and reduce, or eliminate, chances for attachment of the particle to the gas bubble surface.

Because the interactions between particles and bubbles are usually analyzed using experimentally measurable forces instead of energies, we define the Lewis acid-base forces ( $F$ ) interacting between a small particle with a radius  $R$  and a much larger gas bubble (the case of sphere-flat surface interactions) as follows:

$$F = -2\pi R \Delta G_{SLG}^{AB} (l_0) \exp\left(\frac{l_0 - l}{\lambda}\right) \quad \text{Eq. 55}$$

Figure 15 shows the magnitude and range of the Lewis acid-base forces, Lifshitz-van der Waals forces, and electrostatic force operating between a coal particle and a gas bubble. The properties of the system and parameters used in calculating colloidal forces are specified in the figure caption and they were selected arbitrarily based on the literature data presented for coal surfaces by Good et al. [86] and summarized for coal flotation systems by Laskowski [87].

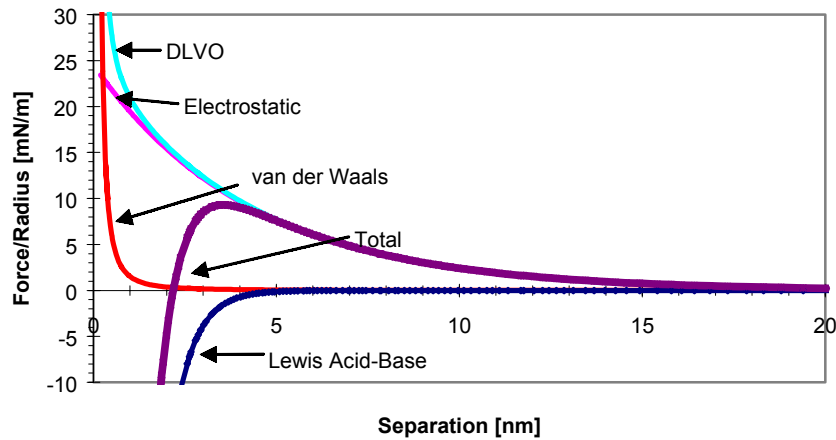


Figure 15. Normalized colloidal forces operating between a coal particle and a gas bubble surface calculated based on DLVO model and Lewis acid-base interactions. Parameters used in calculations are: surface potential of  $-30$  mV for both coal and gas bubble surfaces, concentration of 1:1 electrolyte  $0.005\text{M}$ , which gives the Debye length equal to  $1/\kappa = 4.3$  nm, Hamaker constant  $A_{SLG} = -9 \times 10^{-21}$  J, correlation length for water  $\lambda = 0.6$ , and Lewis acid-base free energy  $\Delta G_{SLG}^{AB} = -70$  mJ/m<sup>2</sup>, calculated by Eq. 53 using experimental data presented in Ref. [86].

It is shown in Figure 15 that DLVO theory predicts a strong repulsion between coal particles and gas bubbles in aqueous solutions of 1:1 electrolytes and therefore attachment of coal particles to gas bubble surface should not occur. Repulsive Lifshitz-van der Waals interactions result from Hamaker constant for coal ( $5.7 \times 10^{-20}$  J; calculated based on data presented in Ref. [86]) that is larger than for water ( $3.7 \times 10^{-20}$  J) and gas ( $\sim 0$  J) [88]. Repulsive electrostatic interactions are caused by negative surface potentials typical for coals and gas bubbles dispersed either in water or aqueous solutions of electrolytes [87]. The only attraction that takes place between a coal particle and a gas bubble comes from “hydrophobicity” of the coal particle and resulting Lewis acid-base interactions. This attraction however, is relatively short range and becomes important at distances shorter than 4-5 nm. As shown in Figure 15, in order for the coal particle to be brought to such a short separation distance and then attach to the gas bubble surface a large energy barrier caused by repulsive electrostatic interactions must be overcome.

Compression of the electrical double layers surrounding the coal particle and gas bubble, for example, by increasing the concentration of electrolyte, can reduce this energy barrier.

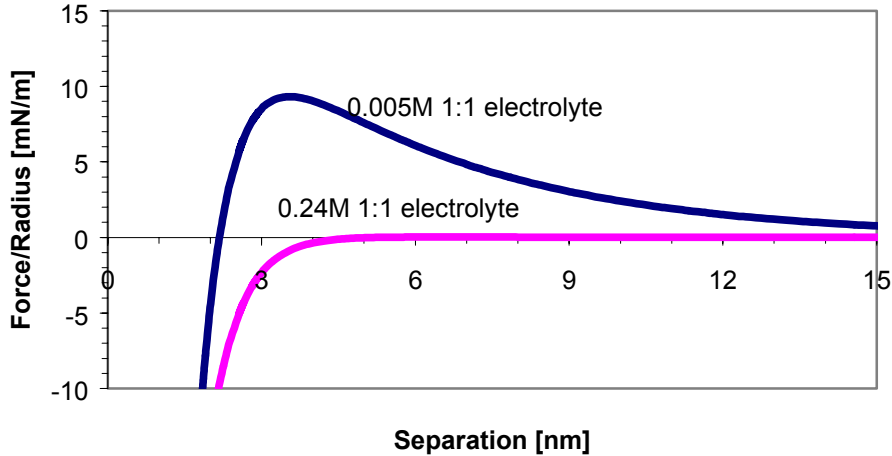


Figure 16. Theoretically calculated force (total of Lifshitz-van der Waals, electrostatic, and Lewis acid-base forces) profile for a coal particle and a gas bubble in aqueous solutions of 1:1 electrolyte of two different concentrations, 0.005M and 0.24 M. Parameters used in calculations are the same as specified in caption of Figure 15.

As calculated for the system under consideration and shown in Figure 16, a concentration of 0.24 M electrolyte is needed to eliminate the energy barrier and promote spontaneous attachment of the coal particle to the gas bubble through attractive “hydrophobic” interactions. This result is consistent with the practical studies of coal flotation, which have shown that many coals can be floated in high-ionic strength salt solutions without any additional reagents [87]. However, as follows, attractive hydrophobic forces can be directly measured at separation distances of more than 100 nm.

#### “Hydrophobic” Forces - Measurements

Hydrophobic attraction forces between macroscopic solid surfaces were experimentally determined for the first time in 1982 [89]. Mica surfaces were rendered moderately hydrophobic by the adsorption of a monolayer of a cationic surfactant, hexadecyltrimethylammonium bromide (or CTAB), from an aqueous solution, giving an advancing water contact angle of about 60° [68, 89]. The measured forces are shown in Figure 17.

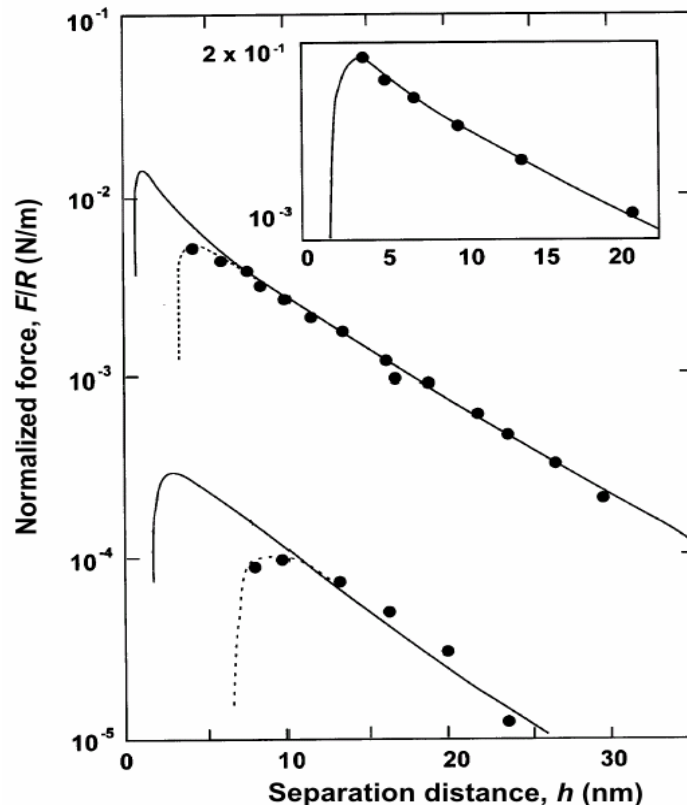


Figure 17. Normalized force  $F/R$  between cylindrically curved hydrophobic surfaces with radius  $R$  as a function of separation distance in  $10^{-3}$  M NaCl and KBr solutions, giving a surface charge density of 1 electron per  $5 \text{ nm}^2$  (upper curve) and 1 electron per  $95 \text{ nm}^2$  (lower curve). Dotted curves describe the difference between the experimental data (points) and the DLVO theory (solid curves). Agreement is observed with hydrophilic (uncoated) mica surfaces (inset) [89].

The next measurements [90] between hydrophobic surfaces, made by adsorption of dihexadecylmethylammonium acetate, showed that the hydrophobic attractive force had a longer range (about 15 nm). The hydrophobic attractive force versus separation distance was again described by a single exponential, but with a larger decay length of 1.4 nm. More hydrophobic surfaces were obtained by depositing a monomolecular layer of dioctadecyldimethylammonium (DODA) bromide onto the mica surface using the Langmuir-Blodgett (LB) technique [69]. The force measurements showed that the hydrophobic attraction extended to 30 nm.

Other experiments with uncharged Langmuir-Blodgett films of hydrocarbon and fluorocarbon surfactants [71] showed some quite startling results. The hydrophobic attractive force was measurable out to a separation distance of 90 nm. The advancing water contact angle was  $113^\circ$  and  $93^\circ$  for the fluorocarbon and DDOA surfaces, respectively. The hydrophobic force was again fitted by a double exponential function. The short-range exponential decay length was from 2 to 3 nm for both surfaces. At longer distances the hydrophobic attraction decayed exponentially with a decay length of 13 nm for hydrocarbon and of 16 nm for fluorocarbon.

Table 6. Experimentally determined values of hydrophobic force constants  $K$  and decay lengths  $\lambda$  reported in the literature

System	$-K$ mN/m	$\lambda$ nm	$-K^*$ mN/m	$\lambda^*$ nm	Contact angle <sup>†</sup>	Reference
Mica-Mica in CTAB solution	140	1.0			65	[89]
Mica-Mica in $2 \times 10^{-5}$ M DHDAA solution	352	1.4			95	[90]
DDOA LB layers in water	100	2.5	1.6	15		[71]
Polymerized LB layers in water	1.7	62				[91]
“ in 1 mM NaBr	0.4	63				
“ in 10 mM NaBr	0.25	42				
DDOA LB layers in water and in $10^{-2}$ M KBr	3.6	1.2	6.6	5.5	94	[69]
Silica-Silica in $1 \times 10^{-5}$ M CTAB	7	6	6	20	75; 46	[92]
DDOA LB layers in $10^{-5}$ M DAH solution	35	2.5			99; 53	[93]
Mica-Mica in $5 \times 10^{-6}$ M DAH	50	1.4			80; 60	[94]
Mica-Mica in $10^{-6}$ M DAH + $5 \times 10^{-7}$ M octanol	40	1.2	0.5	6.8	84; 72	[95]
Mica-Mica in $10^{-6}$ M DAH + $5 \times 10^{-6}$ M octanol	40	1.2	0.5	4.0	84; 65	
Mica-Mica in $10^{-6}$ M DAH + $1 \times 10^{-7}$ M dodecanol	40	1.0			64; 65	
Mica-Mica in $5 \times 10^{-6}$ M DAH + $1 \times 10^{-7}$ M dodecanol	45	1.2	1.2	6.8	88; 80	
Mica-Mica in $5 \times 10^{-6}$ M DAH + $1 \times 10^{-7}$ M dodecanol	45	1.2	1.3	9.0	90; 86	
Mica-Mica in $5 \times 10^{-6}$ M DAH + $5 \times 10^{-7}$ M dodecanol	40	1.2	1.0	2.0	88; 78	
Mica-Mica in $5 \times 10^{-6}$ M DAH + $5 \times 10^{-7}$ M dodecanol	45	1.3			85; 65	
Mica-Mica in $5 \times 10^{-6}$ M DAH + $5 \times 10^{-6}$ M dodecanol						
Mica-Mica in $10^{-5}$ M DAH						
Silanated glass sphere and silanated silica plate with the same hydrophobicity (symmetric interactions)	9.0	2.0			81	[81]
	12	10			92	
	9.0	24			100	
	83	32			109	
	20	2.0			0	
Silanated glass sphere (with a contact angle of $109^\circ$ ) and silanated silica plate with a contact angle given in the 6 <sup>th</sup> column (asymmetric interactions)	9.0	9.0			75	
	12	12			83	
	15	20			92	
	25	22			97	
	30	25			100	
	58	28			105	
	83	32			109	

<sup>†</sup> Advancing and receding contact angle, respectively. DHDAA = dihexadecyldimethylammonium acetate. DDOA = dimethyldioctadecylammonium bromide. DAH = dodecylammonium hydrochloride.

These hydrophobic attractive forces were followed by a large number of experimental studies using the Surface Force Apparatus of Israelachvili [66] as well as the non-interferometric surface force techniques [96, 97], of which the Atomic Force Microscope (AFM) colloidal probe technique [98, 99] is the most popular. A summary of values for the hydrophobic attraction force constants and decay lengths reported by various authors is given in Table 6.

Since these days a vast amount of data for hydrophobic forces measured between solid surfaces has been reported in the literature. All of the surface force measurements indicate that there is a hydrophobic attraction force between hydrophobic solid macroscopic surfaces, in excess of the DLVO forces. The range is quite variable. Smooth hydrophobic surfaces do not show the very long-range attraction. Instead, there is a short-range attraction that is stronger than the van der Waals interaction [100]. For surfaces rendered hydrophobic by a silanation process, very long-range (over 100 nm) attractive forces are observed with the presence of submicroscopic bubbles [79].

To rationalize the available experimental observations, the measured forces can be divided into three categories [101]:

- Short-range, strongly attractive forces between stable surfaces (Type I).
- Attractive forces with variable strength and range in the presence of submicroscopic bubbles (Type II).
- Very long-range, attractive forces with exponential decay (Type III).

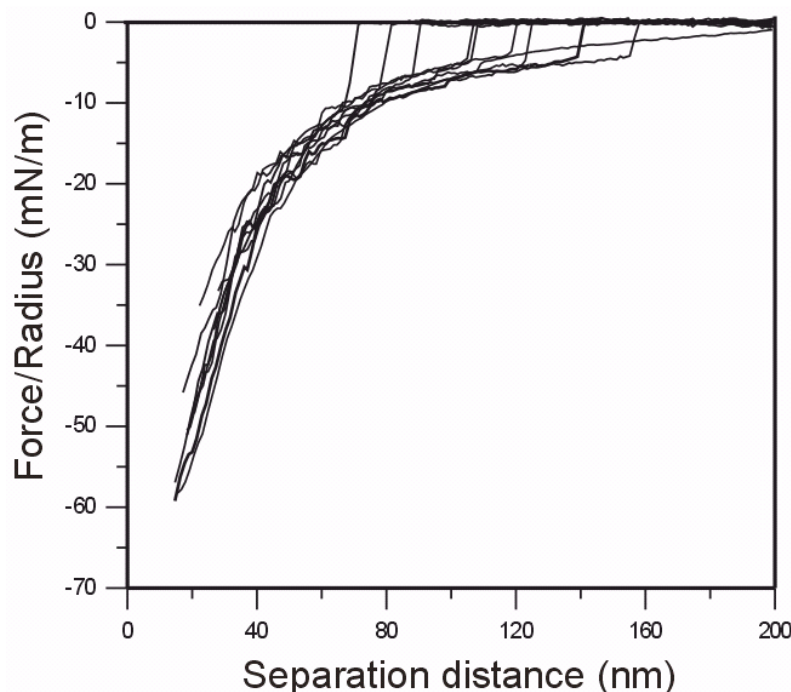


Figure 18. Steps in the force curves between a polyethylene sphere and a silanated silica plate in water saturated by nitrogen[102]

Forces of type I are measured with stable surfaces having an advancing water contact angle greater than  $90^\circ$  and a small hysteresis of contact angle. These hydrophobic surfaces include polymerized LB films chemically grafted to plasma-treated mica surfaces [100] or silica [103], plasma-polymerized films on mica [104], some bulk polymer surfaces [105], thiol-modified gold surfaces [106], fused polystyrene [105], and some silylated surfaces [107]. These hydrophobic forces have a range up to 20 nm, and are not significantly influenced by electrolytes.

Forces of type II are typically measured with glass and silica surfaces rendered hydrophobic by a silanation process in the gas phase [79, 102, 108-110]. The range of these forces is up to a few hundred nanometers. Submicroscopic bubbles at the surfaces coalesce during the surface approach, causing steps in the force curves (Figure 18) and bridging of the surfaces together. The size of the steps on the force curves depends on the gas solubility. However, the measured forces do not depend on the gas solubility significantly. The influence of surface roughness and heterogeneity appear to be quite significant [102].

Forces of type III are measured with many surfaces rendered hydrophobic by surfactant adsorption in situ from aqueous [111-114] or cyclohexane solutions [115, 116], and LB films on mica [69]. The decay length of these exponentially decaying forces varies from about 5 to 50 nm. Added salts can influence forces of type III as ionised surfactants electrostatically adsorb to surfaces. The long-range attractive forces measured between one hydrophobic and one hydrophilic surface [117] can also be placed in this category.

Measurements of the interaction forces between a bubble and a solid particle are only recently possible with the invention of the atomic force microscope [118] and the development of microfabricated cantilevers. In the AFM colloidal probe measurements, the probe particle is glued to the end of the cantilever and the bubble is attached to a flat surface on the AFM piezoelectric transducer, which is used to change the relative position between the bubble and the particle. Deflection of the cantilever and distance of the sample are measured and converted into the interaction force and the relative bubble-particle position [119, 120].

The first measurements using the AFM colloidal probe technique were reported in 1994 [121, 122]. The expected attraction between hydrophobic silica particles was observed. An attractive force observed between hydrophilic particles and bubbles by Ducker et al. [121] was probably due to hydrophobic contamination [119]. The metastable films between a bubble and a dehydroxylated silica sphere were found to have a weak hydrophobic attraction [119]. In the case of more hydrophobic particles, the intervening liquid films drained rapidly and the three-phase contact line was instantly formed, leading to the establishment of a strong adhesive force [122]. In all cases, the results are semi-quantitative since the bubble surface deforms as the particle approaches. Both the bubble deformation and film rupture make the measurement of the hydrophobic force between a bubble and a particle difficult.

Measurement of surface forces shows that the type of surfaces as well as dissolved gases accumulated in the form of submicroscopic gas bubbles have a strong influence on the hydrophobic attraction between solid surfaces, as well as between a bubble and a particle. It is likely that the coalescence between the pre-existing submicroscopic gas bubbles at the solid surface and the large bubble causes the film rupture during the

measurements of force between a bubble and a particle, resulting in the particle-bubble attachment and contact. The importance of gas bubbles ‘precipitating’ on solid surfaces and enhancing mineral flotation, particularly in vacuum flotation, was well known to flotation chemists [123-125]. The key feature of these investigations in bubble formation is the significant role played by the solid surface [109, 110, 126]. Dissolved air and gasses can exist in water in the form of tiny bubbles, down to nanometer dimensions called bubstons (i.e. bubbles stabilised by ions) [127]. The formation of larger bubbles from the pre-existing sources of the bubstons can therefore occur without the need for a nucleation step, which is not energetically favorable.

In flotation, solid particles are generally in contact with air before they have contact with water. Air and gases which are trapped on particle surfaces, especially hydrophobic surfaces, are not easy to be displaced by the surrounding liquid water phase and these air-filled cavities are the pre-existing sites for the ‘bridging’ of gas cavities during the particle-bubble interaction. Particle surface geometry and chemistry are important. Surface geometric defects can act as sites where the gas can be trapped. Shape of the particles (angularity) can stimulate the rupture of the intervening liquid film during the bubble-particle attachment and enhance flotation [128]. Flotation collectors adsorb onto the particle-liquid surface in an uneven fashion. The patchy distribution of these collectors on solid surfaces has been identified [109] and these heterogeneities of the hydrophobic surface can act as sites to trap gas cavities and promote strong attraction between surfaces due to the coalescence and bridging of microscopic gas bubbles.

It is evident that the nature of hydrophobic forces is interconnected with phenomena involving structure of the gas-liquid interfaces, bubble nucleation, submicron bubbles at the surface and how these phenomena influence the stability of water film between bubble and solid hydrophobic surface.

#### **4. Structure and Stability of Water Films at Hydrophobic Surfaces**

##### Structure of water near surfaces

The presence of a solid surface significantly perturbs the structure of the water adjacent to the surface. Likewise, the water is also perturbed at the gas-liquid interface.

The interactions between water molecules and solutes (ionic and nonionic species) having different physicochemical properties prompted a number of investigations into the molecular structure of water and the effects that various solutes (charged and uncharged) may have upon this structure [129]. Like other liquids close to their melting point, water may be considered a disordered solid rather than a dense vapor, with a tetrahedral structure, orderliness, which extends over a distance smaller than about three molecular diameters because of the thermal movements of the strongly polar water molecules.

Thermodynamic and spectroscopic studies [129] have shown that a thermodynamic equilibrium can exist between the bulk water structure and the “dense” solid-like water structure.

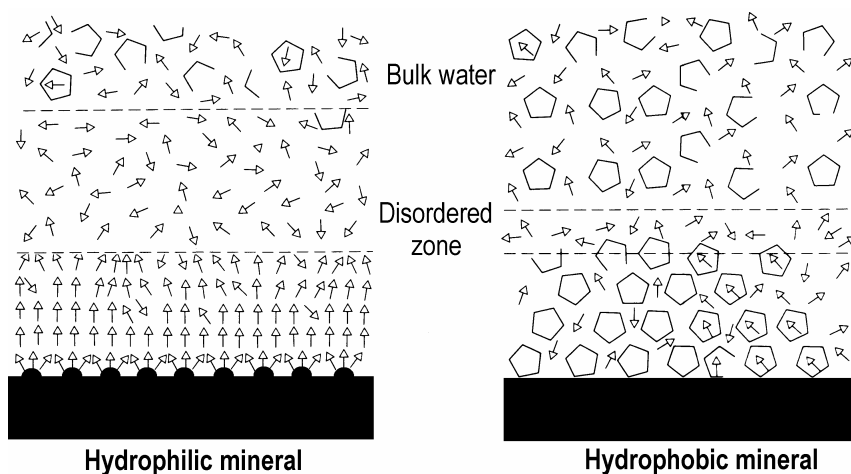


Figure 19. Water structure at hydrophilic and hydrophobic surfaces. Bulk water is shown by pentagonal and partial pentagonal structures, which are in equilibrium with monomeric water represented by arrows. Dipole-dipole interaction at a hydrophilic surface causes ordering of water molecules, leading to a notable disordered zone. Water molecules at a hydrophobic surface have extensive clathrate-like structure with a minimal disordered zone [130].

The equilibrium can be considerably affected by the presence of solid surfaces and the presence of structure-making or structure-breaking compounds. Repulsive hydration forces arise whenever molecules are strongly hydrated or water is strongly bound to hydrophilic surfaces, such as hydrated ions or hydroxyl (-OH) groups, which modify the H-bonding network of liquid water adjacent to them (Figure 19).

The introduction of an apolar molecule or hydrophobic surface into water leads to a reduction in the degrees of freedom – spatial, orientational, dynamic – of the neighboring water molecules. These water molecules become more solid-like (quasi-crystallized). The normal bulk structure of the water molecules is locally absent and an "iceberg" with clathrate-like structure is formed around the apolar residues.

Various techniques have been used to study the ordering of water molecules near hydrophobic interfaces, including the air/water interface. Sum - frequency generation (SFG) [131, 132], Raman [133] and FTIR [134] spectroscopies along with extended X-ray absorption fine structure (EXAFS) [135], neutron reflectivity [136] and X-ray reflectivity [137] have been used. SFG studies of water at air/water, CCl<sub>4</sub>/water and octadecyltrichlorosilane/water interfaces [131, 132] indeed indicated the presence of a broken hydrogen bonds (free OH stretch) near a hydrophobic interface. However, other SFG studies indicated that the hydrogen bonding between adjacent water molecules close to the hydrophobic interface is weak, in contrast to generally accepted models [138]. Nevertheless, interaction between these water molecules and hydrophobic surfaces results in significant orientation of these weakly hydrogen - bonded molecules in the interfacial region. EXAFS [135], neutron reflectivity [136] and X-ray reflectivity [137] studies all indicate an expanded more ordered network of water molecules near hydrophobic surfaces. Molecular dynamic studies also confirmed the results of SFG studies [139].

It is apparent that phenomena occurring at the water-hydrophobic interface are responsible for the observed short - and long - range attractions. It was recently proposed

that the film might become unstable to thermal and mechanical (hydrodynamic) fluctuations and that fluctuating gaps are generated between two hydrophobic interfaces [74]. If fluctuations are large enough, bridging gas cavities can form between such hydrophobic surfaces.

While intermolecular water structure seems to be important for short range hydrophobic forces, the long-range hydrophobic force seems to be related to the stabilization of nanosized gas bubbles at hydrophobic surfaces. Cavitation was indeed experimentally observed in surface force apparatus measurements when two hydrophobic surfaces were separated from contact in water [71]. Optical laser pulse cavitation experiments in thin films bounded by hydrophilic and hydrophobic surfaces indicated significantly higher probability of cavitation near hydrophobic surfaces [127]. Outgassing significantly decreased the probability of cavitation near hydrophobic surfaces but had only a mild influence on cavitation near hydrophilic surfaces. Other indirect evidence for the existence of submicroscopic bubbles at hydrophobic surfaces exists. Miller and coworkers [134] used attenuated total reflectance ATR/FTIR spectroscopy measurements to indicate the presence of gas species at a hydrophobic surface. No accumulation of hydrophobic butane gas at hydrophilic silica surfaces was observed. However, on hydrophobic silicon surfaces, butane was accumulated. Analysis of their spectra suggests that butane was adsorbed in the form of aggregates rather than single molecules.

Direct visualization of nanobubbles at hydrophobic surfaces has recently been achieved. Tyrell and Attard [110, 140] have observed nanobubbles with the tapping mode atomic force microscopy on hydrophobized glass surfaces. Complementary force curves between a silica colloidal probe and a glass surface display features characteristic of the hydrophobic interaction, including a jump - in distance that is comparable to the height of the imaged bubbles. Nanobubbles are not present in ethanol but regrow following the subsequent reintroduction of water. Bubbles with a radius of 100 nm and of irregular shape were observed. Other researchers involved in the research of gas/liquid interfaces recently reported direct observation of very small bubbles on hydrophobic surfaces [126].

Other experimental techniques have recently been used to prove the existence of nanobubbles and their precursor layer at the hydrophobic solid surface [137]. Neutron reflectivity experiments on the interface of pure D<sub>2</sub>O against thin films of predeuterated polystyrene (d-PS) spin - coated onto silicon blocks were performed to study the intrinsic structure of interfacial water at a hydrophobic surface. The experiments revealed the existence of nonvanishing scattering contrast at the water/polymer interface. It was concluded that this represents a precursor layer of submicroscopic bubbles observed in the AFM experiments, which were also performed with the same system. The thickness of this gas precursor layer was 2-5 nm, depending on the level of air saturation of the water sample and on the time elapsed after contacting it with the hydrophobic surface. Neutron reflectivity studies showed that in the presence of gas the thickness of the gas layer near the flat surface is anywhere between 2 and 5 nm [137], depending on the gas supersaturation level. X-ray reflectivity studies with pure outgassed water showed that thickness of the dewetted region extends less than 1.5 nm from the hydrophobic surface [136]. Such a precursor layer might also have a crucial role in bubble nucleation or attachment to hydrophobic surfaces.

Based on these observations and theoretical analysis [141], it has been proposed that the long - range attraction between hydrophobic solids is due to bridging of pre-

existing nanobubbles on hydrophobic surfaces, or bubble nucleation (cavitation) as surfaces approach each other [79], as it is shown on Figure 20. Direct force measurements by numerous researchers [100, 142-145] showed the existence of long-range hydrophobic forces and the diminished attraction in deaerated water.

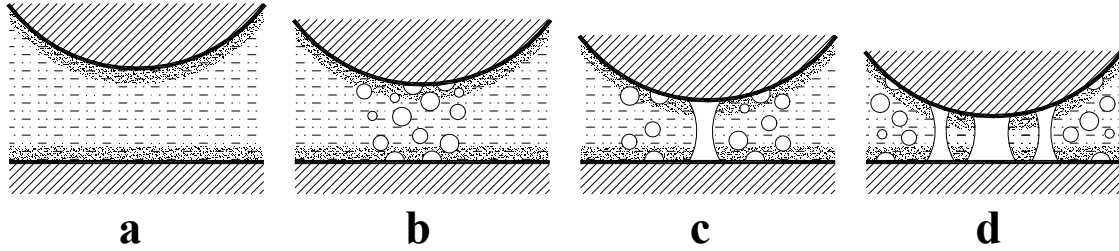


Figure 20. Schematic picture of cavitation phenomena during approach of hydrophobic sphere and hydrophobic plane in water. a) layers of lower medium density (adsorbed gas molecules), b) nanobubbles formation, c) bridging cavity formation, d) multiple bridging cavities, leading to film rupture and attachment

The existence of similar features at the gas-liquid interface is still in debate. It was recently proposed that the stability of macroscopic bubbles in various electrolytes can be explained with the formation of a surface layer of nanobubbles [146]. The relationship between dissolved electrolytes, bubble coalescence, surface tension, gas solubility, and ion hydration was also studied [147-149]. Ninham and coworkers observed a peculiar phenomenon that while some electrolytes stabilized macroscopic bubbles, other did not influence bubble coalescence at all. Moreover, a combination of some cations and anions would always produce stabilization, while a combination of other ions would destabilize bubbles. After careful analysis of the problem, it was proposed that macroscopic bubbles are surrounded with the gradients of submicron bubbles and that such gradients play an important role in the coalescence of macroscopic bubbles. Electrolytes, which are successful in decreasing gas solubility, decrease the concentration and gradient of submicron bubbles and therefore stabilize macroscopic bubbles. On the other hand, the electrolytes that did not influence solubility of a particular gas did not influence the stability of macroscopic bubbles to an appreciable extent. As in the case of surface nanobubbles, supersaturation and slow gas/liquid system equilibration again seem to be responsible for the observed behavior, at least in part.

#### Rupture of Water Film at a Hydrophobic Surface

Macroscopic liquid films on flat solid surfaces are unconditionally stable if the thickness of the liquid film is larger than  $h_{cr}$  [150]:

$$h_{cr} = 2\sqrt{\frac{\gamma}{\rho g}} \sin \frac{\theta}{2} \quad \text{Eq. 56}$$

where  $\gamma$  is the liquid surface tension,  $\rho$  is the liquid density,  $g$  is the gravitational constant, and  $\theta$  is the equilibrium contact angle.

For liquid films that are a few hundred micrometers or less, the gravity is negligible and stability of such films is governed by a competition between interfacial tensions of the solid-liquid-gas system [151]. Sharma and Ruckenstein analyzed the change in free energy of the three-phase system associated with rupture of a uniform liquid film separating a solid surface from a gas phase [151]. They found that the maximum film thickness ( $h_{max}$ ) at rupture depends on the diameter of the hole (hole is referred to a solid area exposed to a gas phase after film rupture) that is formed ( $d$ ) and wetting characteristics of the solid surface defined by equilibrium contact angle ( $\theta$ ) [151]:

$$\frac{4h_{max}}{d \sin \theta} = 1 + \frac{(1 - \cos \theta)^2}{\sin^2 \theta} \exp\left(\frac{-4h_{max}}{d \sin \theta}\right) \quad \text{Eq. 57}$$

It can be concluded from this model that liquid films are less stable when they are spread over macroscopic and microscopic solid surfaces rather than sub-microscopic solid surfaces because only small diameter holes, if energetically favorable, can be formed on sub-microscopic surfaces due to geometrical factor that needs to be taken into account. The same might be true for macroscopic surfaces if the nucleation of holes is governed by roughness and/or heterogeneity characteristics of the solid surface. Also due to equation 57, thinner liquid films remain stable on solid surfaces that possess stronger interactions with wetting liquid.

For a particle interacting with a bubble, the maximum solid-gas area that can be formed after liquid film rupture is usually restricted by the size, shape, topography, and heterogeneity of the particle. In the case of particles that are a few hundreds of micrometers in diameter or smaller, the diameter of the nucleated hole formed on such particles can be several micrometers at most due to restrictions posed by particle geometry. Recent AFM studies indicate that the diameter of the small bubbles nucleated on hydrophobic (heterogeneous) surfaces immersed in water is less than  $0.1 \mu\text{m}$  [126]. These small bubbles not only activate destabilization of the liquid film but probably also represent the size of hydrophobic patches that are responsible for creation of the holes of similar lateral dimensions. Sheludko et al. [6] derived an equation on the critical radius ( $r_c$ ) of the three-phase contact line below which the linear free energy is too large for the three-phase contact line to be stable:

$$r_c = \frac{\sigma}{\gamma(1 - \cos \theta)} \quad \text{Eq. 58}$$

where  $\sigma$  is the line tension,  $\gamma$  is surface tension, and  $\theta$  is contact angle.

Assuming that  $r_c$  is equivalent to the minimum size of the nuclei and holes that can be formed in a liquid film and taking the line tension value as  $10^{-10} \text{ J/m}^2$  [152], equation 58 predicts that the minimum diameter of the three-phase contact area after liquid film rupture is about 30-300 nm, depending on the liquid surface tension and solid wetting characteristics.

Table 7 shows the theoretical values of the maximum thickness of the liquid film at rupture as predicted by the theoretical model proposed by Sharma and Ruckenstein [151]. The  $h_{max}$  values were calculated using equation 57 and assuming that the diameter of the hole is as small as 10  $\mu\text{m}$ , 1  $\mu\text{m}$  or 0.1  $\mu\text{m}$ . The calculations were done for three different equilibrium contact angles of 30, 60, and 90 degrees. As shown in Table 7, if the size of the solid-gas area formed after film rupture is reduced to 10  $\mu\text{m}$  or less, the thickness of the stable liquid film is reduced to a few micrometers. For instance, the maximum thickness of the stable film is reduced to 10-30 nm if the maximum diameter of the formed solid-gas contact area is 100 nm. At such short separations ( $<30$  nm) of one interface (solid-liquid) from another interface (liquid-gas), colloidal forces often operate, as described in previous sections, and the stability of the liquid film is affected (surface tension of the liquid-gas interface might be affected as well). For example, long-range repulsive electrostatic forces enhance the stability of thin water films. These repulsive colloidal forces, if present, provide additional energetic barrier for the liquid film to rupture and slow down, or even eliminate, the attachment of particles to a gas bubble surface. A detailed analysis of the surface forces effect on the critical film thickness is however, beyond the scope of this paper.

Table 7. Prediction of the liquid film thickness at rupture according to equation 57

Critical Diameter of Rupture Hole (d) [ $\mu\text{m}$ ]	Contact angle ( $\theta$ ) [deg]	Maximum Film Thickness ( $h_{max}$ ) [ $\mu\text{m}$ ]
10	30	1.28
	60	2.40
	90	3.19
1	30	0.13
	60	0.24
	90	0.32
0.1	30	0.01
	60	0.02
	90	0.03

### 5. Formation and Relaxation of Three Phase Contact Line

The formation of a three phase contact line during rupture of a liquid film is very rapid process but must be initiated by favorable energetic conditions. As discussed in the previous section, the liquid film ruptures due to energetic imbalance in interfacial tensions of the three-phase system. Because of the small dimensions of the holes nucleated during film rupture, the tension at the three phase contact line can be as important, or even dominating, factor as tensions at surfaces. The formation of the three phase contact line cannot begin from a zero or near zero dimension because of the large work of formation associated with this process [153]. The minimum dimension of the three phase contact line that can be formed has been formulated by Scheludko et al. [6] and presented in the previous section (see equation 58).

Figure 21. Selected frames for an air bubble (~1.5 mm in diameter) attachment at a chalcopyrite surface in deionized water as captured with a Kodak EktaPro 1000 High-Speed Video System (J. Drelich and J.D. Miller – unpublished)

The dynamics of expansion of the three phase contact line after its formation has been extensively studied for high-viscosity polymeric films [154]. Similar studies that involve low-viscosity liquids, important to particle-liquid-bubble systems, are very much in their infancy, mainly due to experimental difficulties to obtain a precise recording of this rapid relaxation process. As an example, Figure 21 shows the event of air bubble attachment to a chalcopyrite surface in deionized water. The sequence of three high-speed video frames in the upper row represents the time of bubble shape stabilization and water film thinning. The lower row of high-speed video frames shows the formation of the three phase contact line and its expansion; from the moment the water film breaks to the final “equilibrium state” when the three phase contact line remains stable. It can be seen that the relaxation of the three phase contact line for the example shown in Figure 21 is completed in about 40 ms.

Hydrodynamic and molecular-kinetic models are the two principal approaches used to describe the dynamics of a liquid spreading (or retreating) over (from) a solid or liquid surface [155]. These models differ by the mode of energy dissipation. Viscous drag within the spreading liquid is responsible for the energy dissipation in the hydrodynamic model. In the molecular-kinetic model, dissipation is the result of friction at the three-phase contact line. Both theories describe the experimental results fairly well for viscous liquids at low and moderate velocities. Due to a lack of experimental data, suitability of theoretical models to explain high velocity relaxation conditions and low viscosity liquids remains unexplored.

The driving force for the three phase contact line expansion over a solid surface comes from the difference between the dynamic ( $\theta_d$ ) and equilibrium ( $\theta_o$ ) contact angles. The velocity of the three phase contact line enlargement ( $dr/dt$ ), for a circular-shape solid-gas area of contact characterized by a radius  $r$ , depends on the difference between the cosine of the dynamic contact angle and the cosine of the equilibrium contact angle [156]:

$$\frac{dr}{dt} \sim \gamma (\cos\theta_o - \cos\theta_d) \quad \text{Eq. 59}$$

Because the difference between  $\theta_d$  and  $\theta_o$  contact angles diminishes with relaxation time, with the dynamic contact angle increasing from zero (or a near zero) value to a static receding contact angle, the velocity of the three phase contact line expansion decreases with progression of the spreading phenomenon. It should be verified experimentally if  $\theta_o$  in the above equation should refer to the equilibrium contact angle, as usually assumed in the literature, or to the static receding contact angle.

## 6. Summary and Conclusions

Substantial progress has been made in our understanding of the interaction of bubbles with solid surfaces. This progress includes analysis of surface hydrodynamic forces, the theoretical examination and measurement of surface forces, and the characterization of interfacial water/solid surface states.

In the case of bubble approach/contact, hydrodynamic force analysis has been successful in description of geometry of the approaching interfaces and their deformation. Film thinning during collision and sliding is well described by approximate solutions for hydrodynamic functions for both no-slip and slip gas-liquid interface.

Even greater advances have been made in the case of surface forces governing film thinning, rupture, and attachment. For example, the significance of the hydrophobic attractive force is well documented. Although not completely understood from a quantitative perspective, it is clear that manifestation of this force is related to the discontinuities in the water film between hydrophobic interfaces. The effect of different variables, including dissolved gas and roughness of the solid surface on this force is well observed.

Finally this progress has been made, in part, due to the ability to more accurately characterize the structures of interfacial water and solid surface states, both spatially with AFM resolution at the nanometer level and spectroscopically with surface sensitivity to describe the vibrational features of interfacial molecules. For example formation of nanobubbles at the solid hydrophobic surfaces has been observed. Spectroscopic studies have shown differences between bulk water structure and the water molecules arrangement at the interfaces.

## 7. References

1. Jameson, G.J., S. Nam, and M.M. Young, *Physical factors affecting recovery rates in flotation*. Minerals Sci. Engng., 1977. **9**: p. 103-118.
2. Schulze, H.J., *Hydrodynamics of bubble-mineral particle collisions*. Miner. Process. Extract. Met. Rev., 1989. **5**: p. 43-76.
3. Yoon, R.H. and G.H. Luttrell, *The effect of bubble size on fine particle flotation*. Miner. Proc. Extract. Met. Rev., 1989. **5**: p. 101-122.
4. Dai, Z., D. Fornasiero, and J. Ralston, *Particle-bubble collision models - a review*. Advances in Colloid and Interface Science, 2000. **85**(2-3): p. 231-256.
5. Nguyen, A.V., *Hydrodynamics of liquid flows around air bubbles in flotation: a review*. International Journal of Mineral Processing, 1999. **56**(1-4): p. 165-205.
6. Scheludko, A., B.V. Toshev, and D.T. Bojadjiev, *Attachment of particles to a liquid surface (capillary theory of flotation)*. J. Chem. Soc., Faraday Trans. 1, 1976. **72**(12): p. 2815-28.
7. Ye, Y., S.M. Khandrika, and J.D. Miller, *Induction-time measurements at a particle bed*. Int. J. Miner. Process., 1989. **25**(3-4): p. 221-40.
8. Schulze, H.J., B. Radoev, T. Geidel, H. Stechemesser, and E. Toepfer, *Investigations of the collision process between particles and gas bubbles in flotation - a theoretical analysis*. Int. J. Miner. Process., 1989. **27**(3-4): p. 263-78.
9. Sutherland, K., *The physical chemistry of flotation XI. Kinetics of the flotation process*. J. Phys. Chem., 1948. **52**: p. 394-425.
10. Dobby, G.S. and J.A. Finch, *Particle collection in columns - gas rate and bubble size effects*. Can. Metall. Q., 1986. **25**(1): p. 9-13.
11. Nguyen, A.V., H.J. Schulze, H. Stechemesser, and G. Zobel, *Contact time during impact of a spherical particle against a plane gas-liquid interface: theory*. International Journal of Mineral Processing, 1997. **50**(1-2): p. 97-111.
12. Huh, C. and L.E. Scriven, *Shapes of axisymmetric fluid interface of unbounded extend*. J. Colloid Interface Sci., 1969. **30**: p. 323-337.
13. Hartland, S. and R.W. Hartley, *Axisymmetric Fluid-Liquid Interfaces: Tables Giving the Shape of Sessile and Pendant Drops and External Menisci, with Examples of Their Use*. 1976, Amsterdam: Elsevier. 782.
14. Poisson, M., *Nouvelle The'orie de l'Action Capillaire*. 1831, Paris: Bachelier.
15. Philippoff, W., *Some dynamic phenomena in flotation*. Trans. Amer. Inst. Min. Engngs. Min. Engng., 1952. **193** (April): p. 386-390.
16. Derjaguin, B.V., *Theory of the distortion of a plane surface of a liquid by small objects and its application to the measurement of the contact angle of the wetting of thin filaments and fibres*. Dokl. Akad. Nauk SSSR, 1946. **51**(7): p. 517-520.
17. Nguyen, A.V., *Empirical Equations for Meniscus Depression by Particle Attachment*. Journal of Colloid and Interface Science, 2002. **249**(1): p. 147-151.
18. Nguyen, A.V. and G.M. Evans, *The Liquid Flow Force on a Particle in the Bubble-Particle Interaction in Flotation*. Journal of Colloid and Interface Science, 2002. **246**(1): p. 100-104.
19. Nguyen, A.V., G.M. Evans, and G.J. Jameson, *Approximate calculations of electrical double-layer interaction between spheres*, in *Encyclopedia of Surface and Colloid Science*, A.T. Hubbard, Editor. 2002, Marcel Dekker: New York.
20. Nguyen, A.V., *Historical note on the Stefan-Reynolds equations*. Journal of Colloid and Interface Science, 2000. **231**(1): p. 195.
21. Scheludko, A., *Zur Flotation Theorie*. Kolloid-Zeitschrift und Zeitschrift für Polymere, 1963. **191**(1): p. 52-58.
22. Manev, E.D., S.V. Sazdanova, and D.T. Wasan, *Emulsion and foam stability - the effect of film size on film drainage*. J. Colloid Interface Sci., 1984. **97**(2): p. 591-4.
23. Radoev, B., A. Scheludko, and E. Manev, *Critical thickness of thin liquid films:*

- theory and experiment*. J. Colloid Interface Sci., 1983. **95**(1): p. 254-65.
24. Schulze, H.J., B. Wahl, and G. Gottschalk, *Determination of adhesive strength of particles within the liquid/gas interface in flotation by means of a centrifuge method*. J. Colloid Interface Sci., 1989. **128**(1): p. 57-65.
  25. Schulze, H.J., K.W. Stockelhuber, and A. Wenger, *The influence of acting forces on the rupture mechanism of wetting films - nucleation or capillary waves*. Colloids and Surfaces, A: Physicochemical and Engineering Aspects, 2001. **192**(1-3): p. 61-72.
  26. Hogg, R., T.W. Healy, and D.W. Fuerstenau, *Mutual coagulation of colloidal dispersions*. Trans. Faraday Soc., 1966. **62**: p. 1638-1651.
  27. Nguyen, A.V. and G.M. Evans, *Axisymmetric approach of a solid sphere toward a non-deformable planar slip interface in the normal stagnation flow--development of global rational approximations for resistance coefficients*. International Journal of Multiphase Flow, 2002. **28**(8): p. 1369-1380.
  28. Cameron, A., *The principles of lubrication*. 1966, London: Longmans. 326.
  29. Goldman, A.J., R.G. Cox, and H. Brenner, *Slow viscous motion of a sphere parallel to a plane wall I. Motion through a quiescent fluid*. Chem. Eng. Sci., 1967. **22**(4): p. 637-51.
  30. Happel, J. and H. Brenner, *Low Reynolds Number Hydrodynamics numbers*. 1991, Dordrecht/Boston/London: Kluwer Academic. 553.
  31. Goldman, A.J., R.G. Cox, and H. Brenner, *Slow viscous motion of a sphere parallel to a plane wall II. Couette flow*. Chem. Eng. Sci., 1967. **22**(4): p. 653-60.
  32. Goren, S.L. and M.E. O'Neill, *Hydrodynamic resistance to a particle of a dilute suspension when in the neighborhood of a large obstacle*. Chem. Eng. Sci., 1971. **26**(3): p. 325-38.
  33. Derjaguin, B., *Untersuchungen ueber die Reibung und Adhaesion IV. Theorie des Anhaften kleiner Teilchen*. Kolloid-Z., 1934. **69**: p. 155-166.
  34. Derjaguin, B. and L. Landau, *Theory of the stability of strongly charged lyophobic sols and of the adhesion of strongly charged particles in solutions of electrolytes*. Acta Phys.-chim., 1941. **14**(6): p. 633-662.
  35. Verwey, E.J.W. and J.T.G. Overbeek, *Theory of the Stability of Lyophobic Colloids*. 1948, Amsterdam: Elsevier. 218.
  36. Pashley, R.M., *Hydration forces between mica surfaces in aqueous electrolyte solutions*. J. Colloid Interface Sci., 1981. **80**(1): p. 153-62.
  37. Israelachvili, J.N., *Forces between surfaces in liquids*. Adv. Colloid Interface Sci., 1982. **16**: p. 31-47.
  38. Derjaguin, B.V., *Structural and thermodynamic peculiarities of the boundary layers of liquids*. Pure Appl. Chem., 1980. **52**(5): p. 1163-78.
  39. Churaev, N.V. and B.V. Deryagin, *Inclusion of structural forces in the theory of stability of colloids and films*. J. Colloid Interface Sci., 1985. **103**(2): p. 542-53.
  40. Israelachvili, J.N., *Intermolecular and Surface Forces*. 1992, London: Academic Press. 291.
  41. Pailthorpe, B.A. and W.B. Russel, *The retarded van der Waals interaction between spheres*. J. Colloid Interface Sci., 1982. **89**(2): p. 563-6.
  42. Lifshitz, E.M., *The theory of molecular attractive forces between solid bodies*. J. Exp. Theor. Phys. USSR, 1955. **29**: p. 83-94.
  43. Mahanty, J.H. and B.W. Ninham, *Colloid Science: Dispersion Forces*. 1977, London: Academic Press. 236.
  44. Nguyen, A.V., G.M. Evans, and H.J. Schulze, *Prediction of van der Waals interaction in bubble-particle attachment in flotation*. International Journal of Mineral Processing, 2001. **61**(3): p. 155-169.
  45. Pashley, R.M. and J.N. Israelachvili, *DLVO and hydration forces between mica surfaces in magnesium(2+), calcium(2+), strontium(2+), and barium(2+) chloride solutions*. J. Colloid Interface Sci., 1984. **97**(2): p. 446-55.

46. Ney, P., *Zeta-Potentiale und Flotierbarkeit von Mineralien*. 1973, Wien: Springer Verlag.
47. Li, C. and P. Somasundaran, *Reversal of bubble charge in multivalent inorganic salt solutions-effect of magnesium*. J. Colloid Interface Sci., 1991. **146**(1): p. 215-18.
48. Li, C. and P. Somasundaran, *Reversal of bubble charge in multivalent inorganic salt solutions - effect of aluminum*. J. Colloid Interface Sci., 1992. **148**(2): p. 587-91.
49. Li, C. and P. Somasundaran, *Reversal of bubble charge in multivalent inorganic salt solutions-effect of lanthanum*. Colloids Surf., A, 1993. **81**(1-3): p. 13-15.
50. Yoon, R.H. and J.L. Yordan, *Zeta-potential measurements on microbubbles generated using various surfactants*. J. Colloid Interface Sci., 1986. **113**(2): p. 430-8.
51. Laskowski, J.S., J.L. Yordan, and R.H. Yoon, *Electrokinetic potential of microbubbles generated in aqueous solutions of weak electrolyte type surfactants*. Langmuir, 1989. **5**(2): p. 373-6.
52. Taggart, H.A., *The electrification of liquid-gas surfaces*. Philoso. Mag., 1914. **27 (6th Ser.)**: p. 297-315.
53. Saulnier, P., P. Bouriat, G. Morel, J. Lachaise, and A. Graciaa, *Zeta potential of air bubbles in solutions of binary mixtures of surfactants*. J. Colloid Interface Sci., 1998. **200**: p. 81-85.
54. Dibbs, H.P., L.L. Sirois, and R. Bredin, *Some electric properties of bubbles and their role in the flotation of quartz*. Canadian Metall. Quart., 1974. **13**: p. 395-404.
55. Graciaa, A., G. Morel, P. Saulnier, J. Lachaise, and R.S. Schechter, *The zeta potential of gas bubbles*. J. Colloid Interface Sci., 1994. **172**: p. 131-136.
56. McShea, J.A. and I.C. Callaghan, *Electrokinetic potentials at the gas-aqueous interface by spinning cylinder electrophoresis*. Colloid & Polymer Sci., 1983. **261**: p. 757-766.
57. Cichos, C., *Effect of the electrokinetic potentials of air bubbles and mineral particles on flotation results*. Freiberg. Forschungsh. A, 1973. **513**: p. 7-28.
58. Usui, S. and H. Sasaki, *Zeta potential measurements of bubbles in aqueous surfactant solutions*. J. Colloid Interface Sci., 1978. **65**(1): p. 36-45.
59. Olphen, v.H., *An introduction to clay colloid chemistry*. 1977, New York: Wiley. 367.
60. Pashley, R.M., *Hydration forces between mica surfaces in electrolyte solutions*. Adv. Colloid Interface Sci., 1982. **16**: p. 57-62.
61. Marcelja, S. and N. Radic, *Repulsion of interfaces due to boundary water*. Chem. Phys. Lett., 1976. **42**(1): p. 129-30.
62. Landau, L.D. and E.M. Lifshitz, *Statistical Physics*. 2 ed. 1975, Oxford: Pergamon. 618.
63. Gruen, D.W.R., S. Marcelja, and V.A. Parsegian, *Water structure near the membrane surface*. Recept. Ligands Intercell. Commun., 1984. **3**(Cell Surf. Dyn.): p. 59-91.
64. Schiby, D. and E. Ruckenstein, *The role of the polarization layers in hydration forces*. Chem. Phys. Lett., 1983. **95**(4-5): p. 435-8.
65. Rabinovich, Y.I., B.V. Derjaguin, and N.V. Churaev, *Direct measurements of long-range surface forces in gas and liquid media*. Adv. Colloid Interface Sci., 1982. **16**: p. 63-78.
66. Israelachvili, J.N. and G.E. Adams, *Direct measurement of long range forces between two mica surfaces in aqueous potassium nitrate solutions*. Nature (London), 1976. **262**(5571): p. 774-7.
67. Leikin, S., V.A. Parsegian, D.C. Rau, and R.P. Rand, *Hydration forces*. Annu. Rev. Phys. Chem., 1993. **44**: p. 369-95.
68. Israelachvili, J.N. and R.M. Pashley, *Measurement of the hydrophobic interaction*

- between two hydrophobic surfaces in aqueous electrolyte solutions. *J. Colloid Interface Sci.*, 1984. **98**(2): p. 500-14.
69. Claesson, P.M., C.E. Blom, P.C. Herder, and B.W. Ninham, *Interactions between water-stable hydrophobic Langmuir-Blodgett monolayers on mica*. *J. Colloid Interface Sci.*, 1986. **114**(1): p. 234-42.
  70. Eriksson, J.C., S. Ljunggren, and P.M. Claesson, *A phenomenological theory of long-range hydrophobic attraction forces based on a square-gradient variational approach*. *J. Chem. Soc., Faraday Trans. 2*, 1989. **85**(3): p. 163-76.
  71. Claesson, P.M. and H.K. Christenson, *Very long range attractive forces between uncharged hydrocarbon and fluorocarbon surfaces in water*. *Journal of Physical Chemistry*, 1988. **92**(6): p. 1650-5.
  72. Yaminskii, V.V., V.S. Yushchenko, E.A. Amelina, and E.D. Shchukin, *Cavity formation due to a contact between particles in a nonwetting liquid*. *J. Colloid Interface Sci.*, 1983. **96**(2): p. 301-6.
  73. Christenson, H.K. and P.M. Claesson, *Cavitation and the interaction between macroscopic hydrophobic surfaces*. *Science (Washington, D. C., 1883-)*, 1988. **239**(4838): p. 390-2.
  74. Ruckenstein, E. and N.V. Churaev, *A possible hydrodynamic origin of the forces of hydrophobic attraction*. *J. Colloid Interface Sci.*, 1991. **147**(2): p. 535-8.
  75. Podgornik, R. and V.A. Parsegian, *Forces between CTAB-Covered Glass Surfaces Interpreted as an Interaction-Driven Surface Instability*. *J. Phys. Chem.*, 1995. **99**(23): p. 9491-6.
  76. Attard, P., *Long-range attraction between hydrophobic surfaces*. *Journal of Physical Chemistry*, 1989. **93**(17): p. 6441-4.
  77. Rabinovich, Y.I., D.A. Guzonas, and R.H. Yoon, *Role of chain order in the long-range attractive force between hydrophobic surfaces*. *Langmuir*, 1993. **9**(5): p. 1168-70.
  78. Rabinovich, Y.I. and B.V. Deryagin, *Interaction of hydrophobized filaments in aqueous electrolyte solutions*. *Colloids and Surfaces*, 1988. **30**(3-4): p. 243-51.
  79. Parker, J.L., P.M. Claesson, and P. Attard, *Bubbles, cavities, and the long-ranged attraction between hydrophobic surfaces*. *Journal of Physical Chemistry*, 1994. **98**(34): p. 8468-80.
  80. Attard, P., *Bridging Bubbles between Hydrophobic Surfaces*. *Langmuir*, 1996. **12**(6): p. 1693-5.
  81. Yoon, R.-H., D.H. Flinn, and Y.I. Rabinovich, *Hydrophobic interactions between dissimilar surfaces*. *J. Colloid Interface Sci.*, 1997. **185**(2): p. 363-370.
  82. Van Oss, C.J., R.J. Good, and M.K. Chaudhury, *The role of van der Waals forces and hydrogen bonds in hydrophobic interactions between biopolymers and low energy surfaces*. *Journal of Colloid & Interface Science*, 1986. **111**: p. 378-390.
  83. van Oss, C.J., *Interfacial Forces in Aqueous Media*. 1994, New York: Marcel Dekker, Inc.
  84. Giese, F.G. and C.J. van Oss, *Colloid and Surface Properties of Clays and Related Minerals*. 2002, New York: Marcel Dekker, Inc.
  85. Della Volpe, C. and S. Siboni, *Acid-base behavior of (polymer) surfaces: theory*, in *Encyclopedia of Surface and Colloid Science*. 2002, Marcel Dekker, Inc.: New York. p. A17-A36.
  86. Good, R.J., N.R. Srivatsa, M. Islam, H.T.L. Huang, and C.J. van Oss, *Theory of the acid-base hydrogen bonding interactions, contact angles, and the hysteresis of wetting: application to coal and graphite surface*. *Journal of Adhesion Science & Technology*, 1990. **4**: p. 607-617.
  87. Laskowski, J.S., *Coal flotation and fine coal utilisation*. 2001, Amsterdam: Elsevier. 371.
  88. Israelachvili, J.N., *Intermolecular and Surface Forces*. 1991, New York: Academic Press. 291 pp.

89. Israelachvili, J. and R. Pashley, *The long-range hydrophobic interaction decaying exponentially with distance*. Nature (London), 1982. **300**(5890): p. 341.
90. Pashley, R.M., P.M. McGuiggan, B.W. Ninham, and D.F. Evans, *Attractive forces between uncharged hydrophobic surfaces: direct measurements in aqueous solution*. Science (Washington, D. C., 1883-), 1985. **229**(4718): p. 1088-9.
91. Kurihara, K., S. Kato, and T. Kunitake, *Very strong long range attractive force between stable hydrophobic monolayers of a polymerized ammonium surfactant*. Chem. Lett. (Japan), 1990. **9**: p. 1555-1558.
92. Craig, V.S.J., B.W. Ninham, and R.M. Pashley, *Study of the Long-Range Hydrophobic Attraction in Concentrated Salt Solutions and Its Implications for Electrostatic Models*. Langmuir, 1998. **14**(12): p. 3326-3332.
93. Herder, P.C., *Forces between hydrophobed mica surfaces immersed in dodecylammonium chloride solution*. J. Colloid Interface Sci., 1990. **134**(2): p. 336-45.
94. Yoon, R.-H. and S.A. Ravishankar, *Application of extended DLVO theory III. Effect of octanol on the long-range hydrophobic forces between dodecylamine-coated mica surfaces*. J. Colloid Interface Sci., 1994. **166**(1): p. 215-24.
95. Yoon, R.-H. and S.A. Ravishankar, *Long-range hydrophobic forces between mica surfaces in dodecylammonium chloride solutions in the presence of dodecanol*. J. Colloid Interface Sci., 1996. **179**(2): p. 391-402.
96. Craig, V.S.J., *An historical review of surface force measurement techniques*. Colloids and Surfaces, A: Physicochemical and Engineering Aspects, 1997. **129,130**: p. 75-94.
97. Froberg, J.C., O.J. Rojas, and P.M. Claesson, *Surface forces and measuring techniques*. International Journal of Mineral Processing, 1999. **56**(1-4): p. 1-30.
98. Ducker, W.A., T.J. Senden, and R.M. Pashley, *Direct measurement of colloidal forces using an atomic force microscope*. Nature (London), 1991. **353**(6341): p. 239-41.
99. Ducker, W.A., T.J. Senden, and R.M. Pashley, *Measurement of forces in liquids using a force microscope*. Langmuir, 1992. **8**(7): p. 1831-6.
100. Wood, J. and R. Sharma, *How Long Is the Long-Range Hydrophobic Attraction?* Langmuir, 1995. **11**(12): p. 4797-802.
101. Christenson, H.K. and P.M. Claesson, *Direct measurements of the force between hydrophobic surfaces in water*. Advances in Colloid and Interface Science, 2001. **91**(3): p. 391-436.
102. Nguyen, A.V., J. Nalaskowski, J.D. Miller, and H.-J. Butt, *Attraction between hydrophobic surfaces studied by atomic force microscopy*. Inter. J. Miner. Process., 2003. **72**(1-4): p. 215-225.
103. Ohnishi, S., V.V. Yaminsky, and H.K. Christenson, *Measurements of the Force between Fluorocarbon Monolayer Surfaces in Air and Water*. Langmuir, 2000. **16**(22): p. 8360-8367.
104. Parker, J.L., P.M. Claesson, J.-H. Wang, and H.K. Yasuda, *Surface Forces between Plasma Polymer Films*. Langmuir, 1994. **10**(8): p. 2766-73.
105. Schmitt, F.J., T. Ederth, P. Weidenhammer, P. Claesson, and H.J. Jacobasch, *Direct force measurements on bulk polystyrene using the bimorph surface forces apparatus*. J. Adhes. Sci. Technol., 1999. **13**(1): p. 79-96.
106. Kokkoli, E. and C.F. Zukoski, *Interactions between Hydrophobic Self-Assembled Monolayers. Effect of Salt and the Chemical Potential of Water on Adhesion*. Langmuir, 1998. **14**(5): p. 1189-1195.
107. Ishida, N., N. Kinoshita, M. Miyahara, and K. Higashitani, *Effects of Hydrophobizing Methods of Surfaces on the Interaction in Aqueous Solutions*. J. Colloid Interface Sci., 1999. **216**(2): p. 387-393.
108. Carambassis, A., L.C. Jonker, P. Attard, and M.W. Rutland, *Forces Measured between Hydrophobic Surfaces due to a Submicroscopic Bridging Bubble*. Phys.

- Rev. Lett., 1998. **80**(24): p. 5357-5360.
109. Nalaskowski, J., S. Veeramasesaneni, J. Hupka, and J.D. Miller, *AFM measurements of hydrophobic forces between a polyethylene sphere and silanated silica plates. The significance of surface roughness*. Journal of Adhesion Science and Technology, 1999. **13**(12): p. 1519-1533.
  110. Tyrrell, J.W.G. and P. Attard, *Atomic force microscope images of nanobubbles on a hydrophobic surface and corresponding force-separation data*. Langmuir, 2002. **18**(1): p. 160-167.
  111. Christenson, H.K., P.M. Claesson, and R.M. Pashley, *The hydrophobic interaction between macroscopic surfaces*. Proc. - Indian Acad. Sci., Chem. Sci., 1987. **98**(5-6): p. 379-89.
  112. Christenson, H.K., P.M. Claesson, J. Berg, and P.C. Herder, *Forces between fluorocarbon surfactant monolayers: salt effects on the hydrophobic interaction*. Journal of Physical Chemistry, 1989. **93**(4): p. 1472-8.
  113. Herder, P.C., *Interactions between mica surfaces in dodecyl- and octylammonium chloride solutions*. J. Colloid Interface Sci., 1990. **134**(2): p. 346-56.
  114. Yoon, R.H. and S.A. Ravishankar, *Long-Range Hydrophobic Forces between Mica Surfaces in Alkaline Dodecylammonium Chloride Solutions*. J. Colloid Interface Sci., 1996. **179**(2): p. 403-411.
  115. Tsao, Y.H., S.X. Yang, D.F. Evans, and H. Wennerstroem, *Interactions between hydrophobic surfaces. Dependence on temperature and alkyl chain length*. Langmuir, 1991. **7**(12): p. 3154-9.
  116. Tsao, Y.H., D.F. Evans, and H. Wennerstroem, *Long-range attractive force between hydrophobic surfaces observed by atomic force microscopy*. Science (Washington, D. C., 1883-), 1993. **262**(5133): p. 547-50.
  117. Claesson, P.M., P.C. Herder, C.E. Blom, and B.W. Ninham, *Interactions between a positively charged hydrophobic surface and a negatively charged bare mica surface*. J. Colloid Interface Sci., 1987. **118**(1): p. 68-79.
  118. Binnig, G., C. Quate, and C. Gerber, *Atomic force microscope*. Phys. Rev. Lett., 1986. **56**(9): p. 930-933.
  119. Fielden, M.L., R.A. Hayes, and J. Ralston, *Surface and Capillary Forces Affecting Air Bubble-Particle Interactions in Aqueous Electrolyte*. Langmuir, 1996. **12**(15): p. 3721-3727.
  120. Preuss, M. and H.-J. Butt, *Direct measurement of forces between particles and bubbles*. International Journal of Mineral Processing, 1999. **56**(1-4): p. 99-115.
  121. Ducker, W.A., Z. Xu, and J.N. Israelachvili, *Measurements of Hydrophobic and DLVO Forces in Bubble-Surface Interactions in Aqueous Solutions*. Langmuir, 1994. **10**(9): p. 3279-89.
  122. Butt, H.-J., *A technique for measuring the force between a colloidal particle in water and a bubble*. J. Colloid Interface Sci., 1994. **166**(1): p. 109-17.
  123. Taggart, A.F., *Handbook of Ore Dressing*. 1927, New York: John Wiley & Sons.
  124. Gaudin, A.M., *Flotation*. 1957, New York: McGraw-Hill.
  125. Klassen, V.I. and V.A. Mokrousov, *An Introduction to the Theory of Flotation*. 1963, London: Butterworths. 493.
  126. Yang, J., J. Duan, D. Fornasiero, and J. Ralston, *Very Small Bubble Formation at the Solid-Water Interface*. Journal of Physical Chemistry B, 2003. **107**(25): p. 6139-6147.
  127. Bunkin, N.F., O.A. Kiseleva, A.V. Lobeyev, T.G. Movchan, B.W. Ninham, and O.I. Vinogradova, *Effect of Salts and Dissolved Gas on Optical Cavitation near Hydrophobic and Hydrophilic Surfaces*. Langmuir, 1997. **13**(11): p. 3024-3028.
  128. Anfruns, J.F. and J.A. Kitchener, *Rate of capture of small particles in flotation*. Trans. - Inst. Min. Metall., Sect. C, 1977. **86**(March): p. 9-15.
  129. Franks, F., *Water*. 1984, London: The Royal Society of Chemistry. 96.
  130. Drost-Hansen, W., *Structure of water near solid interface*. Ind. Eng. Chem., 1978.

- 61: p. 10-47.
131. Du, Q., E. Freysz, and Y.R. Shen, *Surface vibrational spectroscopic studies of hydrogen bonding and hydrophobicity*. Science (Washington, D. C., 1883-), 1994. **264**(5160): p. 826-8.
  132. Gragson, D.E. and G.L. Richmond, *Comparisons of the Structure of Water at Neat Oil/Water and Air/Water Interfaces As Determined by Vibrational Sum Frequency Generation*. Langmuir, 1997. **13**(18): p. 4804-4806.
  133. Nickolov, Z.S., J.C. Earnshaw, and J.J. McGarvey, *Water structure at interfaces studied by total internal reflection Raman spectroscopy*. Colloids and Surfaces, A: Physicochemical and Engineering Aspects, 1993. **76**(1-3): p. 41-9.
  134. Miller, J.D., Y. Hu, S. Veeramasoneni, and Y. Lu, *In-situ detection of butane gas at a hydrophobic silicon surface*. Colloids and Surfaces, A: Physicochemical and Engineering Aspects, 1999. **154**(1-2): p. 137-147.
  135. Wilson, K.R., R.D. Schaller, D.T. Co, R.J. Saykally, B.S. Rude, T. Catalano, and J.D. Bozek, *Surface relaxation in liquid water and methanol studied by x-ray absorption spectroscopy*. Journal of Chemical Physics, 2002. **117**(16): p. 7738-7744.
  136. Jensen, T.R., M. Ostergaard Jensen, N. Reitzel, K. Balashev, G.H. Peters, K. Kjaer, and T. Bjornholm, *Water in Contact with Extended Hydrophobic Surfaces: Direct Evidence of Weak Dewetting*. Physical Review Letters, 2003. **90**(8): p. 086101/1-086101/4.
  137. Steitz, R., T. Gutberlet, T. Hauss, B. Kloesgen, R. Krastev, S. Schemmel, A.C. Simonsen, and G.H. Findenegg, *Nanobubbles and their precursor layer at the interface of water against a hydrophobic substrate*. Langmuir, 2003. **19**(6): p. 2409-2418.
  138. Raymond, E.A., T.L. Tarbuck, M.G. Brown, and G.L. Richmond, *Hydrogen-bonding interactions at the vapor/water interface investigated by vibrational sum-frequency spectroscopy of HOD/H<sub>2</sub>O/D<sub>2</sub>O mixtures and molecular dynamics simulations*. Journal of Physical Chemistry B, 2003. **107**(2): p. 546-556.
  139. Morita, A. and J.T. Hynes, *A theoretical analysis of the sum frequency generation spectrum of the water surface. Part 2. Time-dependent approach*. Journal of Physical Chemistry B, 2002. **106**(3): p. 673-685.
  140. Tyrrell, J.W.G. and P. Attard, *Images of Nanobubbles on Hydrophobic Surfaces and Their Interactions*. Physical Review Letters, 2001. **87**(17): p. 176104/1-176104/4.
  141. Attard, P., *Thermodynamic Analysis of Bridging Bubbles and a Quantitative Comparison with the Measured Hydrophobic Attraction*. Langmuir, 2000. **16**(10): p. 4455-4466.
  142. Meagher, L. and V.S.J. Craig, *Effect of Dissolved Gas and Salt on the Hydrophobic Force between Polypropylene Surfaces*. Langmuir, 1994. **10**(8): p. 2736-42.
  143. Considine, R.F., R.A. Hayes, and R.G. Horn, *Forces Measured between Latex Spheres in Aqueous Electrolyte: Non-DLVO Behavior and Sensitivity to Dissolved Gas*. Langmuir, 1999. **15**(5): p. 1657-1659.
  144. Mahnke, J., J. Stearnes, R.A. Hayes, D. Fornasiero, and J. Ralston, *The influence of dissolved gas on the interactions between surfaces of different hydrophobicity in aqueous media. Part I. Measurement of interaction forces*. Phys. Chem. Chem. Phys., 1999. **1**(11): p. 2793-2798.
  145. Ishida, N., M. Sakamoto, M. Miyahara, and K. Higashitani, *Attraction between Hydrophobic Surfaces with and without Gas Phase*. Langmuir, 2000. **16**(13): p. 5681-5687.
  146. Weissenborn, P.K. and R.J. Pugh, *Surface tension of aqueous solutions of electrolytes: relationship with ion hydration, oxygen solubility, and bubble coalescence*. J. Colloid Interface Sci., 1996. **184**(2): p. 550-563.

147. Craig, V.S.J., B.W. Ninham, and R.M. Pashley, *Effect of electrolytes on bubble coalescence*. Nature (London), 1993. **364**(6435): p. 317-19.
148. Craig, V.S.J., B.W. Ninham, and R.M. Pashley, *The effect of electrolytes on bubble coalescence in water*. Journal of Physical Chemistry, 1993. **97**(39): p. 10192-7.
149. Weissenborn, P.K. and R.J. Pugh, *Surface Tension and Bubble Coalescence Phenomena of Aqueous Solutions of Electrolytes*. Langmuir, 1995. **11**(5): p. 1422-6.
150. Lamb, H., *Statics*. 1916, London: Cambridge University Press.
151. Sharma, A. and E. Ruckenstein, *Dewetting of solids by the formation of holes in macroscopic liquid films*. Journal of Colloid and Interface Science, 1989. **133**(2): p. 358-68.
152. Drelich, J., *The significance and magnitude of the line tension in three-phase (solid-liquid-fluid) systems*. Colloids and Surfaces, A: Physicochemical and Engineering Aspects, 1996. **116**(1/2): p. 43-54.
153. Nguyen, A.V., J. Ralston, and H.J. Schulze, *On modeling of bubble-particle attachment probability in flotation*. International Journal of Mineral Processing, 1998. **53**(4): p. 225-249.
154. Geoghegan, M. and G. Krausch, *Wetting at polymer surfaces and interfaces*. Progress in Polymer Science, 2002. **28**(2): p. 261-302.
155. Petrov, J.G., J. Ralston, M. Schneemilch, and R.A. Hayes, *Dynamics of Partial Wetting and Dewetting of an Amorphous Fluoropolymer by Pure Liquids*. Langmuir, 2003. **19**(7): p. 2795-2801.
156. Schulze, H.J., *Flotation as a heterocoagulation process: possibilities of calculating the probability of flotation*, in *Coagulation and Flocculation - Theory and Application*, B. Dobias, Editor. 1993, Marcel Dekker: New York. p. 321-353.